Contributions to HiLiftPW-3 Using Structured, Overset Grid Methods

James G. Coder[1]
University of Tennessee, Knoxville, TN 37996

Thomas H. Pulliam[2] and James C. Jensen[3]
NASA Ames Research Center, Moffett Field, CA 94035

The High-Lift Common Research Model (HL-CRM) and the JAXA Standard Model (JSM) were analyzed computationally using both the OVERFLOW and LAVA codes for the third AIAA High-Lift Prediction Workshop. Geometry descriptions and the test cases simulated are described. With the HL-CRM, the effects of surface smoothness during grid projection and the effect of partially sealing a flap gap were studied. Grid refinement studies were performed at two angles of attack using both codes. For the JSM, simulations were performed with and without the nacelle/pylon. Without the nacelle/pylon, evidence of multiple solutions was observed when a quadratic constitutive relation is used in the turbulence modeling; however, using time-accurate simulation seemed to alleviate this issue. With the nacelle/pylon, no evidence of multiple solutions was observed. Laminar-turbulent transition modeling was applied to both JSM configuration, and had an overall favorable impact on the lift predictions.

Nomenclature

AR	=	wing aspect ratio
b	=	span
C_p	=	pressure coefficient
C_D	=	drag coefficient
C_L	=	lift coefficient
C_M	=	pitching-moment coefficient
c	=	chord
M	=	Mach number
N	=	total number of grid points
Re	=	Reynolds number based on reference chord length
S	=	reference wing area
x	=	x-coordinate direction
y	=	y-coordinate direction
α	=	angle of attack
η	=	non-dimensional spanwise coordinate, $2y/b$
Subscripts		
∞	=	free-stream conditions

I. Introduction

ACCURATE prediction of high-lift aerodynamic behavior is a critical aspect in the design and analysis of aircraft. Whether it be maneuvering flight, such as for fighter-type aircraft, or the landing configuration of a commercial transport, the maximum lift coefficient drives the sizing of the main wing. Consequently, this feeds back into the cruise performance through the planform area of the wing. With a wide variety of non-linear, interacting flow physics

---

[1] Assistant Professor, Department of Mechanical, Aerospace and Biomedical Engineering, Senior Member, AIAA.
[2] Research Scientist, Associate Fellow, AIAA.
[3] Research Scientist, Member, AIAA.

present in high-lift aerodynamic flows, it is often preferred to predict them using a computational fluid dynamics (CFD) methodology. Due to the high-Reynolds numbers associated with full-scale systems, these simulations are generally restricted to either Reynolds-averaged Navier-Stokes (RANS) or hybrid RANS/large-eddy-simulation (LES) approaches. This introduces a dependency on the choice of turbulence model, which are generally erratic/inconsistent in predicting smooth-body flow separation. Moreover, the geometric complexities of high-lift systems lead to coarser-than-desired meshes and/or geometric simplifications to fit within available computing resources.

The AIAA High-Lift Prediction Workshop series was organized to assess the state-of-the-art in numerical prediction capabilities for commercial-transport-type aircraft in landing and/or takeoff configurations and to promote improvements to modeling and simulation capabilities [1]. For the first workshop (HiLiftPW-1), held in Chicago, IL in 2010, the focus was the three-element NASA Trap Wing geometry, which had been experimentally evaluated in the NASA Langley 14- by 22-Foot Subsonic Wind Tunnel. In HiLiftPW-1, it was observed that geometric fidelity in the CFD modeling impacted the lift, as including the support brackets decreased the predicted lift. Choice of turbulence model and the use of the thin-layer approximation had a major effect on the flow near the tip [1]. In a follow-on special session, it was observed that including laminar-turbulent transition effects had a positive impact on the lift predictions [2].

The second workshop (HiLiftPW-2) was held in San Diego, CA in 2013 and focused on the DLR-F11 configuration [3]. From the participant results, it was observed that geometric fidelity again had an impact on the predicted lift, with the inclusion of slat brackets and flap-track fairings lowering the predicted maximum lift and the inclusion of pressure-tube bundles altering the character of the flow field [3]. Transition modeling was included from some participants; however, it had a less substantial impact for the DLR-F11 than it had for the Trap Wing in HiLiftPW-1 [4].

The third and most recent workshop, HiLiftPW-3, was held in Denver, CO in 2017 [5]. For this, two high-lift configurations were studied: the NASA High Lift Common Research Model (HL-CRM) [6] and the JAXA Standard Model (JSM) [7,8]. As the HL-CRM has not yet been wind-tunnel tested, the results presented in HiLiftPW-3 are completely predictive based on the specified conditions. The JSM, however, has been tested [7,8], providing an experimental reference for comparisons. Both unstructured and structured, overset grids were provided by the organizing committee for the two configurations.

This paper describes the collaborative structured, overset efforts from NASA and the University of Tennessee, Knoxville using the LAVA (NASA) and OVERFLOW (NASA and Tennessee) computational fluid dynamics codes for HiLiftPW-3. Both codes and the specific modeling approaches used are described, as are the HL-CRM and JSM geometries, grids, and test cases for the workshop. Results are presented and discussed for the baseline modeling approach along with variations in the modeling strategy, including turbulence model variant, the effects of transition modeling, and the use of time-accurate simulations.

II. Geometry and Test Cases

A. High-Lift Common Research Model (HL-CRM)

The NASA High Lift Common Research Model (HL-CRM) [6] is a wing-body high lift system in a nominal landing configuration (slat and flaps deployed at 30° and 37°, respectively) without nacelle, pylon, tail, or support brackets. The development of the HL-CRM was motivated by the success of the Common Research Model (CRM) [9]. The CRM has become a standard for both the experimental and CFD modeling community where it represents a public domain physically consistent geometry which has been used in numerous workshops (the DPW series [10-12], high-order workshop series and here the HiLiftPW3 [5]) and is currently a standard for a number of experiments across the international community. The HL-CRM was developed by Boeing (see, Ref. [6]), as a representative high lift configuration with many of the characteristics of the CRM, but designed as a high lift system. The fully configuration is pictured in Fig. 1; however, for the workshop, the nacelle/pylon were not included. Details of the various design criteria and geometry decisions can be found in Ref. [6].

American Institute of Aeronautics and Astronautics

Figure 1. High-Lift Common Research Model configuration [6].

The HL-CRM was also chosen by the 1st AIAA Geometry and Mesh Generation Workshop (GMGW-1) [13] to assess the current state-of-the art in geometry preprocessing and mesh generation technology and software as applied to aircraft and spacecraft systems. The GMGW-1 participants generate the participant grids for the HiLiftPW3 HL-CRM test cases. Issues associated with grid generation and flow solution in the presence of open and partially sealed geometric gaps between the inboard and outboard flaps, and between the inboard flap and side of body prompted both workshops to include cases to evaluate increments and effects on the required cases. The HL-CRM cases presented here used the committee-provided grids from the workshop website [13]. The grids were generated following the workshop guidelines and details of the surface modeling and volume grid generation are found in Chan [14], where there are extensive descriptions of the process for generating the workshop grids.

One aspect of the grid generation process presented in [14], which has a profound effect on the results presented below, involves the surface modeling and in particular, the use of the provided Computer Aided Design (CAD) geometry definitions to develop the surface grids. The geometry definition for the High Lift CRM is provided in five different formats: three native CAD (Computer Aided Design) formats in NX, CREO, and Parasolid files, and two vendor neutral formats in STEP (Standard for the Exchange of Product model data) and IGES (Initial Graphics Exchange Specification) files. For the current work, the STEP file format was selected as the starting point. The ANSA software package [15] is used to create a discrete representation of the geometry in the form of an unstructured surface triangulation over each geometric component (e.g., fuselage, wing, slat, inboard flap, and outboard flap). Since this surface triangulation will serve as the reference geometry for structured surface grid generation, care is taken to ensure high curvature regions, such as leading edges, are well resolved. Surface features such as sharp edges and component intersection curves typically appear as boundaries of CAD patches in the geometry representation. Chan (Ref) details the process of developing the surface grid, but part of the process requires a projection back to the fine surface triangulation. Using these best practices and the guidelines of the HiLiftPW3 workshop a family of grids was generated and provided to the participants.

Characteristics of the overset grids used for the workshop simulations (labeled "A-HLCRM_StrOverset_ChimeraGridTools(V3)") are provided in Table 1. For the full-chord flap gap, four grid-refinement levels are available, whereas with partially sealed flap gap, only one grid-refinement level is available. As will be shown in the results below, the process of projecting back to the fine triangulation introduces slope and curvature discontinuities, which are attributed to the faceting effect of the surface triangles. This is reflected in unsmooth surface pressure profiles, especially in the leading-edge regions of the slat, wing and flap grids. The projection process was modified to project the surface grid onto the IGES geometry definition (using the Pointwise "project" function), rather than onto a fine triangulation based on the STEP geometry definition. A new set of grids have been posted on the HiLiftPW3 website (labeled "A-HLCRM_StrOverset_ChimeraGridTools(V4)") with the same dimensions as the V3 grids.

American Institute of Aeronautics and Astronautics

The original results presented at the HiLiftPW3 employed the V3 grids, new results show below (and submitted in the final data call post-workshop) used the V4 grids.

Table 1. Grid refinement levels for committee-provided HL-CRM structured, overset grids.

Grid Level	Nodes	Cells	Blocks
Full-Chord Flap Gap			
Coarse	24,059,957	23,097,216	72
Medium	65,423,213	63,537,195	72
Fine	189,285,377	185,201,725	76
X-fine	564,889,833	554,060,880	102
Partially Sealed Flap Gap			
Medium	66,269,520	64,364,621	73

The test cases for the HL-CRM were defined with the intent to analyze the full-scale configuration at wind-tunnel-like conditions. In essence, this can be regarded as analyzing the aircraft with a more viscous fluid so that a lower Reynolds number can be realized without changing the physical dimensions or Mach number. The conditions for the test cases are given in Table 2, and the specified cases are:

- Case 1a (requested): Full-Chord Flap Gap grid-refinement study
- Case 1b (optional): Full-Chord Flap Gap with grid adaptation
- Case 1c (optional): Partially Sealed Chord Flap Gap for medium-resolution grid only
- Case 1d (optional): Partially Sealed Chord Flap Gap with grid adaptation

All simulations were to be run fully turbulent and in free-air (i.e. without wind-tunnel walls). The grid adaptation cases were to be performed with automatic solution adaptation and/or solution-guided grid generation. The authors for this paper only provided results for Case 1a and Case 1c for the HL-CRM.

Table 2. Flow conditions for the HL-CRM (Case 1).

Free-stream Mach Number	0.2
Angles of Attack	8° and 16°
Mean Aerodynamic Chord (MAC)	275.8 in (full scale)
Reynolds Number (based on MAC)	3.26×10^6
Reference Static Temperature	518.67 °R (288.15 K)
Reference Static Pressure	14.700 psi (760.21 mm-Hg)

B. JAXA Standard Model (JSM)

The JAXA Standard Model (JSM) was designed to be representative of a typical 100-person class regional airliner with modern a high-lift system (slat and flap deployed at 25° and 35°, respectively). This geometry was designed to be as representative of a real aircraft as possible, so it includes details such as a flow-through nacelle, flap track fairings, and slat attachment brackets. In order to study the effects of having a nacelle and pylon installed the nacelle-pylon assembly was removable. This allowed for both a nacelle/pylon off (Case 2a) and nacelle/pylon on (Case 2c) version of the geometry which is shown in Figure 2. More details on the exact specifications of the model can be found in [7,8].

Experimental data were made available by the HiLiftPW-3 committee for the both the nacelle-on and nacelle-off versions of the JSM. These are available in Refs. [7] and [8], and include:

4

American Institute of Aeronautics and Astronautics

- Forces and moments through stall
- Surface pressure distributions at multiple spanwise locations on the slat, main element, and flap
- Surface oil-flow images showing upper-surface separation patterns
- Transition locations as determined using China clay

The experiments were run in a 6.5-m by 5.5-m wind tunnel with an estimated turbulence intensity of 0.16%. The model installation featured a 60-mm peniche with an additional 10-mm space between the peniche and fuselage to mitigate measuring forces on the peniche [8].
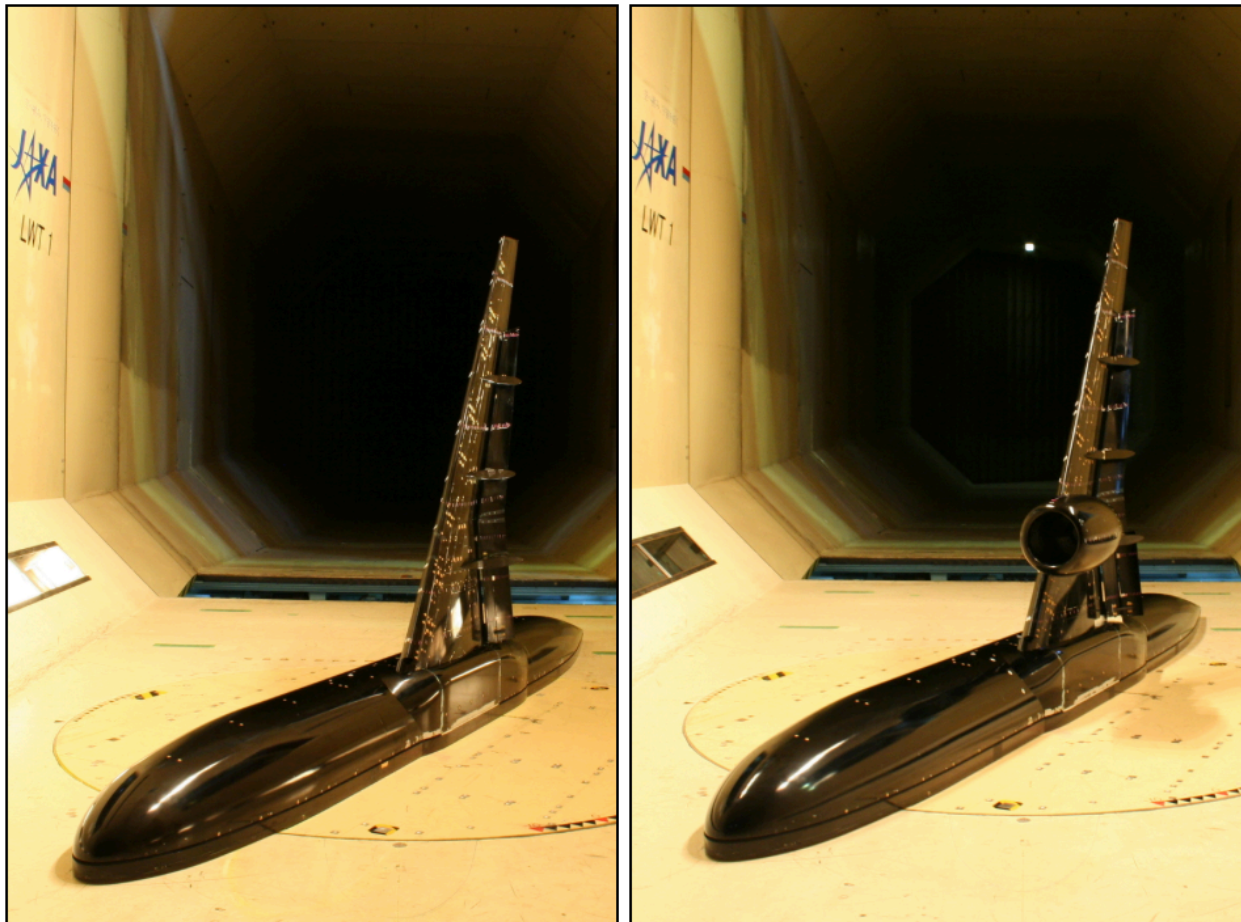
(a) Nacelle/Pylon Off   (b) Nacelle/Pylon On

Figure 2. JAXA Standard Model wind-tunnel configurations [JSMref].

The JSM cases presented here use the provided committee grids (labeled "A-JSM_StrOverset_ChimeraGridTools") from the workshop website [13]. The grids were generated following the workshop guidelines and more details on the mesh generation process for both JSM configurations can be found in Jensen [16]. The reference conditions for the JSM test cases are given below in Table 3, and the specified cases are:

- Case 2a (requested): Nacelle/Pylon Off
- Case 2b (optional): Nacelle/Pylon Off with grid adaptation
- Case 2c (requested): Nacelle/Pylon On
- Case 2d (optional): Nacelle/Pylon On with grid adaptation

All cases were to be run in free air (i.e. without wind-tunnel walls) and either fully turbulent, with predicted transition, or specified transition locations.

5

American Institute of Aeronautics and Astronautics

Table 3. Flow conditions for the JSM (Case 2).

Free-stream Mach Number	0.172
Angles of Attack	4.36°, 10.47°, 14.54°, 18.58°, 20.59°, and 21.57°
Mean Aerodynamic Chord (MAC)	529.2 mm (model scale)
Reynolds Number (based on MAC)	1.93×10^6
Reference Static Temperature	551.79 °R (306.55 K)
Reference Static Pressure	14.458 psi (747.70 mm-Hg)

III. Computational Approach

A. Solvers
OVERFLOW 2.2

OVERFLOW 2.2 is a structured, overset Reynolds-average Navier-Stokes computational fluid dynamics code [17]. It features a variety of spatial discretizations, ranging from 2nd-order central to 5th-order WENO upwind, as well as multiple implicit algorithms for temporal advancement. For attaining steady-state solutions, the code is generally run with locally varying timesteps, but can also be run in a time-accurate manner with a uniform global timestep and either Newton or dual-time subiterations to reduce the implicit linearization errors [18]. Multiple turbulence models are implemented in the code, including the one-equation Spalart-Allmaras model [19], along several enhancements such as streamline rotation and curvature corrections [20] and a non-linear constitutive relation [21], and it also features laminar-turbulent transition prediction capabilities. For the workshop, the baseline method of running OVERFLOW was to use a 3rd-order MUSCL scheme with Roe upwind fluxes, low-Mach preconditioning, and the SA-noft2-RC-QCR2000 variant of the Spalart-Allmaras turbulent model. These simulations were run non-time-accurately towards steady state with grid sequencing to accelerate solution convergence. Overset domain connectivity was calculated using C3P for the HL-CRM cases and with Pegasus 5 for the JSM cases.

In addition to predicting the forces and moments using the baseline modeling approach, three variations in the approach were explored to assess their impact on the predictions: time accuracy, turbulence model variant, and laminar-turbulent transition modeling. Time-accurate simulations were conducted using the 2nd-order backward finite difference scheme with dual-timestepping. The global time step was chosen such that the unsteady residual generally converged by 2 orders of magnitude within 10-20 subiterations. The additional turbulence model variants used are SA-noft2 and SA-noft2-RC. The transition model used was the AFT model of Coder and Maughmer [22] and Coder [23]. Specifically, a new variant, termed AFT2017b, was employed in conjunction with the SA-RC-QCR2000 turbulence model (SA-RC-QCR2000-AFT2017b). The definition of this transition model is provided in the Appendix.

LAVA

The LAVA solver framework [24] offers highly flexible meshing options and was developed with the intent of modeling highly complex geometry and flow-fields. The framework supports Cartesian and curvilinear structured grids as well as unstructured arbitrary polyhedral meshes. Overset grid technology [25] is used to couple the solutions across different overlapping meshes. In this study, the structured curvilinear overlapping grid methodology is applied. The compressible Reynolds Averaged Navier-Stokes (RANS) equations are solved using a finite-difference formulation applied to the non-orthogonal curvilinear transformed system of equations. The finite differencing was performed using the 2nd order modified Roe scheme with the Van Albada limiter. The Spalart-Allmaras (SA) turbulence model was utilized along with its Rotational Correction (RC) [20] and Quadratic Constitutive Relation (QCR2000) [21] variants. The domain connectivity that was used for the LAVA simulations varied depending on the case. For Case 1 the committee provided C3P connectivity was used, for Case 2 the minimum hole was obtained by running OVERFLOW's DCF routines and then inflating the hole boundaries using the Modified Implicit Hole Connectivity (MIHC) routine within LAVA.

For all of the cases LAVA was run in steady state mode using cold starts; meaning that for each angle of attack that was simulated the flow always started from the same initial conditions (no restarting). The solver would run

anywhere from 8 to 48 hours, depending on the mesh, until it reached the desired tolerance within the drag (within a tenth of a drag count 0.00001, or until it showed oscillatory behavior that would not dampen out completely.

B. Computing Resources

All flow solutions presented by the authors in the workshop and in this paper were obtained using the NASA Advanced Supercomputing (NAS) Pleiades cluster. Pleiades is an SGI ICE system featuring over 11,000 compute nodes (over 245,000 cores) with Intel Xeon processors (Broadwell, Haswell, Ivy Bridge, and Sandy Bridge architecture). OVERFLOW simulations were generally run on 420 cores (fully turbulent) and 560 cores (transitional). Steady-state solutions required 24-48 hours of wall-clock time per case, whereas the unsteady simulations required 96 hours of wall-clock time. LAVA simulations required 2,000 cores with 48 hours of wall-clock time per case.

IV. Results

Results for both the HL-CRM and JSM configurations are described below, and encompass solution data submitted for the workshop as well as new solutions for comparison purposes in this paper. The baseline modeling approach for both configurations and both codes is non-time-accurate solutions obtained using the SA-RC-QCR2000 turbulence model. As each solver considered only one discretization, and the same grid systems are used for both, the individual datasets according to the convention "Solver-TurbulenceModel-QCR-Transition-TimeAccuracy". For example, a time-accurate solution obtained using OVERFLOW with the SA-RC-QCR2000-AFT2017b model would be called "OF-SARC-QCR-Trans-TA". The datasets included in this paper are summarized below in Table 4.

A. HL-CRM

Detailed results for the HL-CRM OVERFLOW cases can be found in the summary presentations from the HiLiftPW3 Workshop. In general, the OVERFLOW results were consistent with most of the participants. In this paper, for the HL-CRM cases, we will focus on a few of the more interesting details from the computations.

1. Surface Smoothness Issues

As mentioned above, the original best practice for developing the participant grids involves a projection process back to some truth geometry. In the original posted grids, the process of projection the expert-created surfaces grids back to the fine surface triangulation produced Non-Smooth Surface definitions. A new set of Smooth Surface grids were created by projecting directly back to the CAD definition and produced smoother surface definitions. Figure 3 shows comparisons of pressure coefficient (C_p) at one span station. Looking at the center figure which is a full chord view of the C_p, both grid systems seem consistent. But, looking at detailed pressures at the leading edge of the wing and flap, we see oscillatory pressures on the Non-Smooth surface and smooth results from the Smooth surface. These improvements on the new grid system are consistent across all the grid levels and angles of attack.
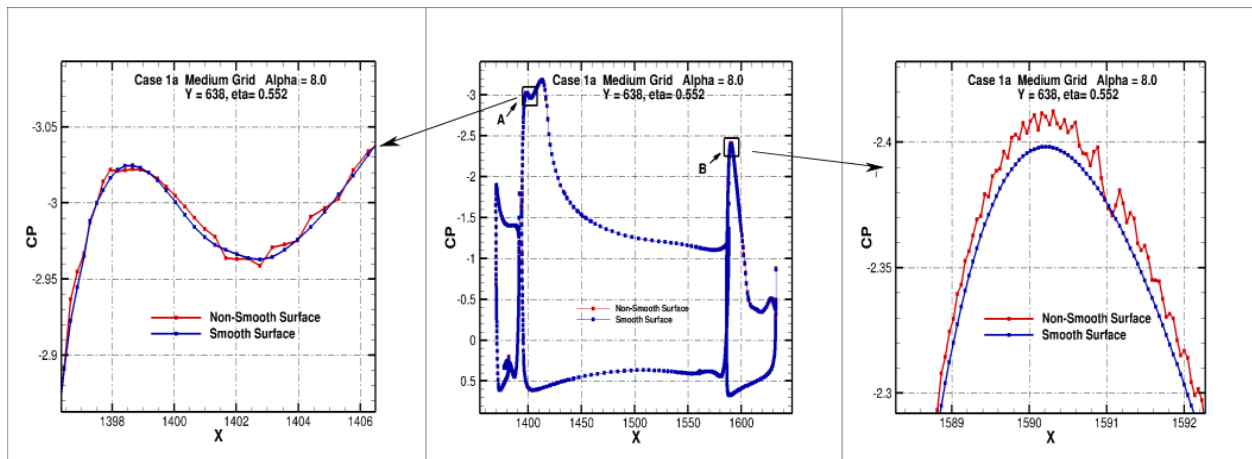
Figure 3. Effect of surface smoothness on surface pressure distribution for the HL-CRM.

2. Turbulence Modeling Effects

American Institute of Aeronautics and Astronautics

The effect of using Quadratic-Constitutive-Relation (QCR) [21] is well documented in various paper and over the last few DPW workshops [10-12]. Typically, the use of QCR results in improved results in corner flow separated regions. Also, the use of rotation (and curvature) corrections (RC) [20] is widespread and well documented for improving the simulation of rotational flows, in particular, corner or juncture flows where boundary layers merge. The gap region of the two-segment flap in the HL-CRM is a prime candidate for these two model corrections and results in Fig. 4 show velocity profiles at the required locations for the workshop. The exclusion of QCR2000 shows the biggest effect in this region. The profile in the gap region on the inboard part of the outboard flap ($X = 1527$, $Y = 443$) shows a small effect outside the boundary layer from excluding RC and QCR. The effect of QCR is more evident on the outboard portion of the inboard flap ($X = 1521$, $Y = 427$), where straight SA-noft2 shows a significantly different velocity profile. Figures 5 and 6 shows surface streamlines which indicate differing separation patterns for the three model variations. Figure 6b shows a close-up view in the flap gap region. There the straight SA-noft2 model shows little to no separated flow, while the addition of QCR and RC produce significant swirling separated flow patterns.
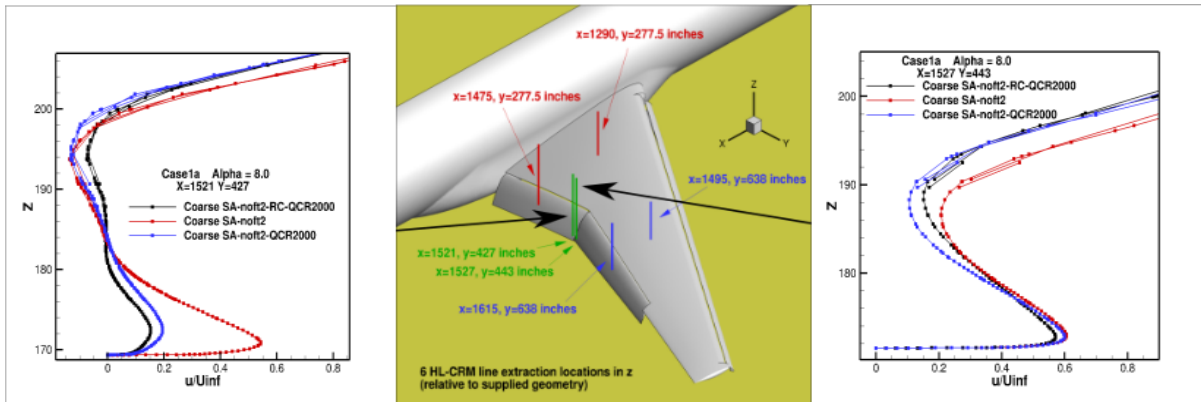
Figure 4. Effect of turbulence model on the predicted velocity profile near the HL-CRM flap gap.
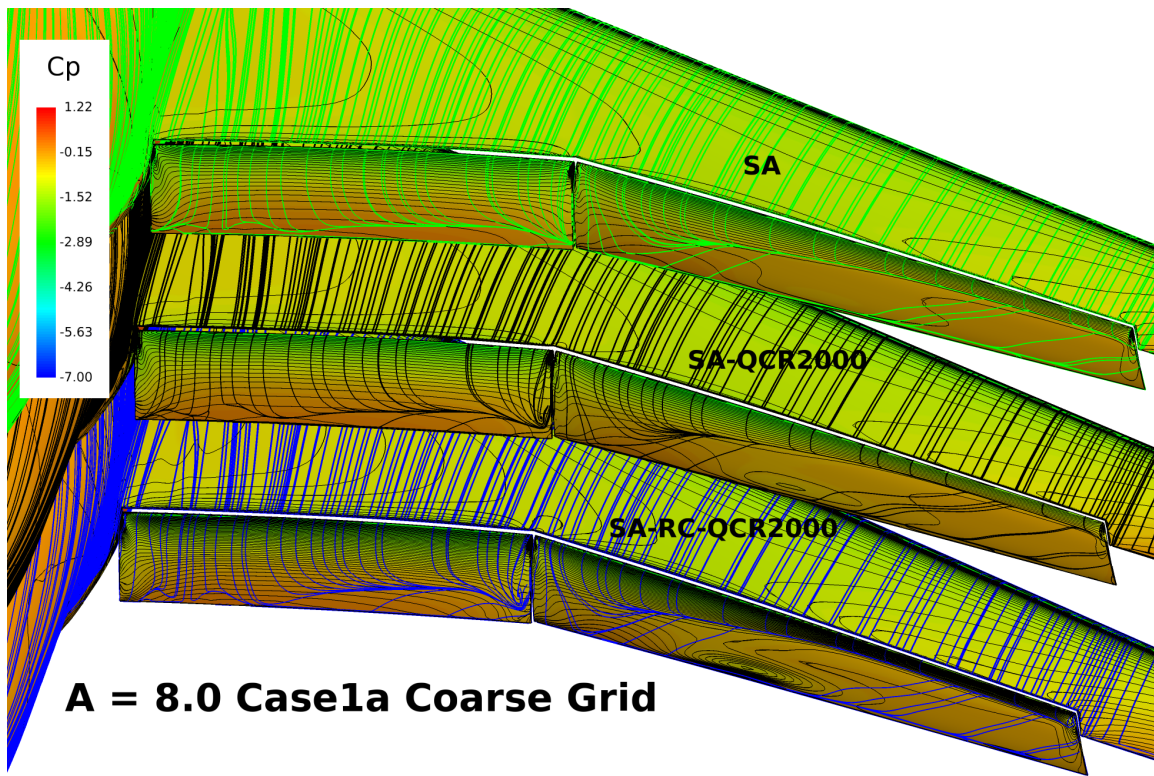
Figure 5. Effect of turbulence model on upper-surface streamlines and separation patterns.

8

SA: Green Lines
SA-QCR: Black Lines
SA-RC-QCR2000: Blue Lines

A = 8.0 Case1a Coarse Grid

(a) Wide view

SA: Green Lines
SA-QCR: Black Lines
SA-RC-QCR2000: Blue Lines

A = 8.0 Case1a Coarse Grid
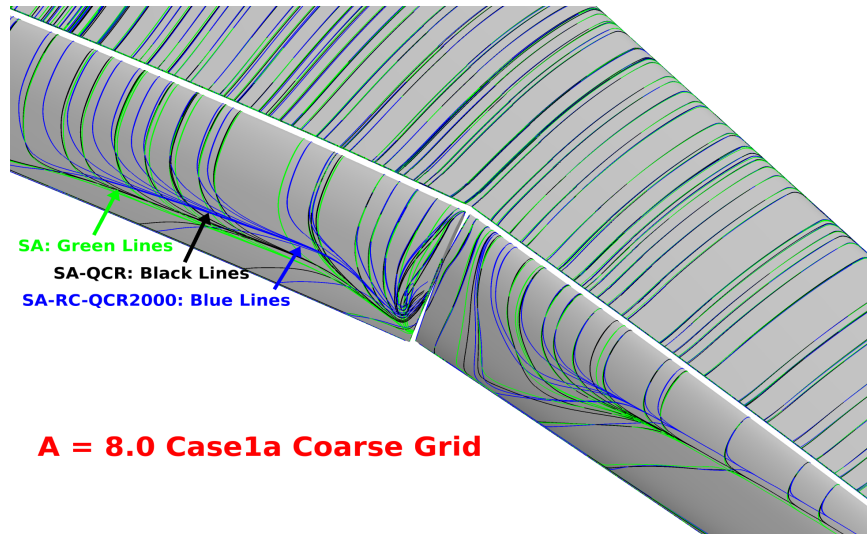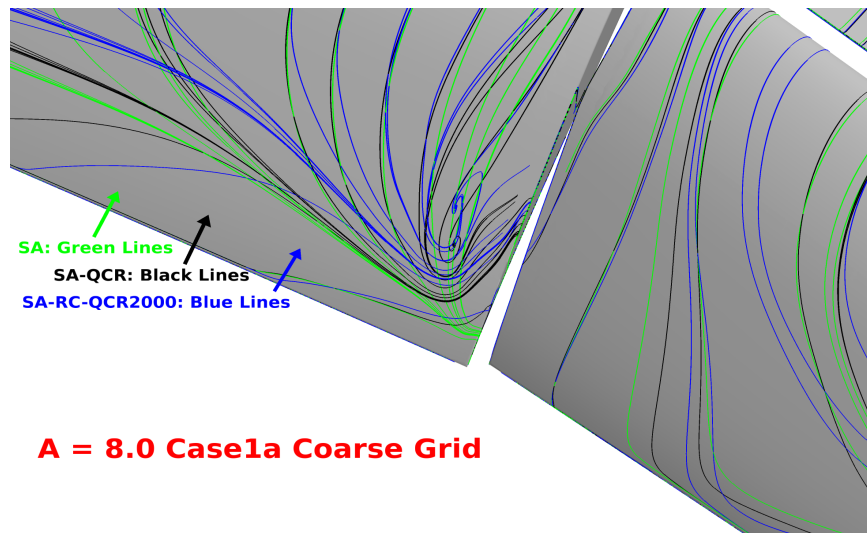
(b) Close-up

Figure 6. Effect of turbulence model on streamlines and separation patterns near the HL-CRM flap gap.

3. Grid Refinement Study (Case 1)

All four structured, overset grid levels with run using LAVA (with the SA model) and OVERFLOW (with the SA-noft2-RC-QCR2000 model) for both 8° and 16° angles of attack. The convergence of the lift, drag, and pitching-moment coefficients are plotted in Fig. 7. Neither solver exhibited true monotonic convergence, and the LAVA results exhibited higher lift, higher drag, and more negative pitching moment. These behaviors are more likely due to the variation in the turbulence modeling between the solvers than differences between the solvers themselves. Predicted surface pressure distributions at select locations on the wing are shown in Figs. 8 and 9 for $\alpha = 8°$ and 16°, respectively, from both codes. There are few variations between the different grid-refinement levels and the two codes; however, two locations stand out. First, for the mid-span location at $\alpha = 8°$

American Institute of Aeronautics and Astronautics

(a) $\alpha = 8°$ (b) $\alpha = 16°$
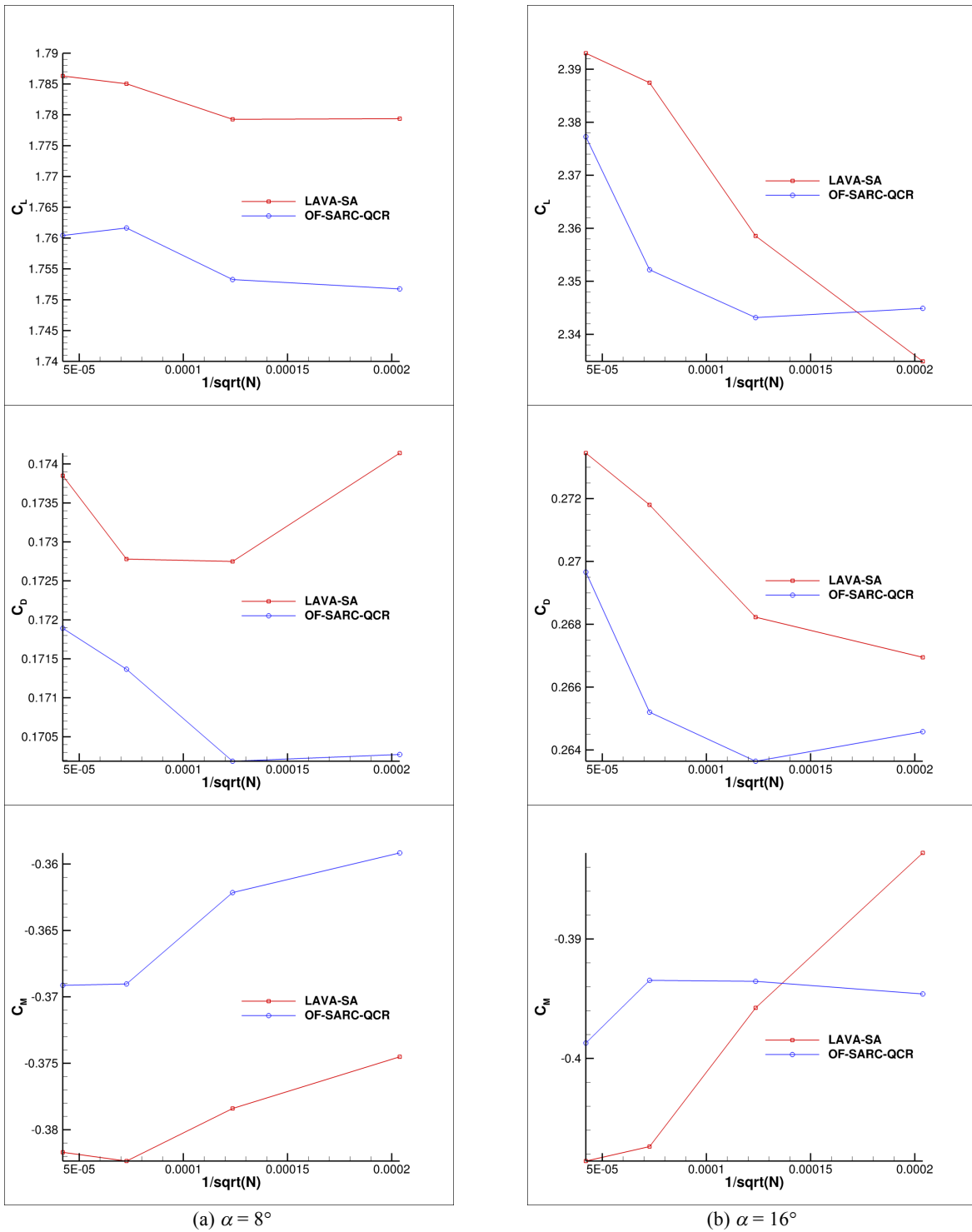
Figure 7. Grid-refinement study of HL-CRM on force and moment coefficients for OVERFLOW and LAVA.

American Institute of Aeronautics and Astronautics
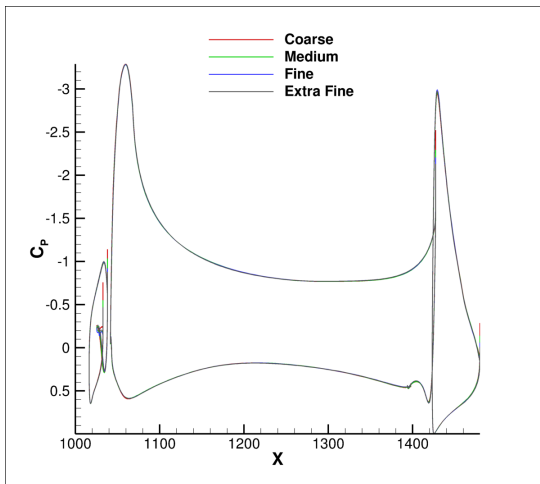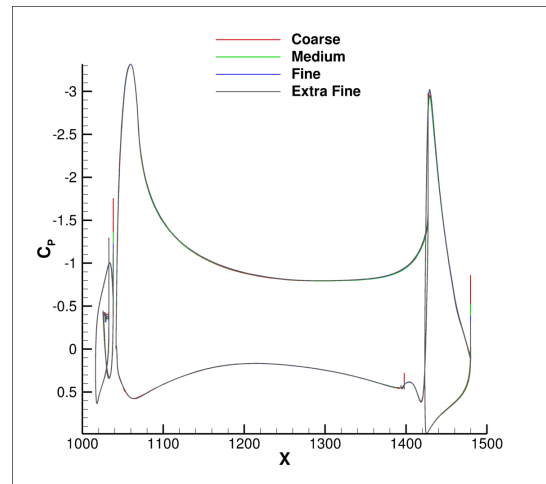
(a) $\eta = 0.151$ (OVERFLOW)
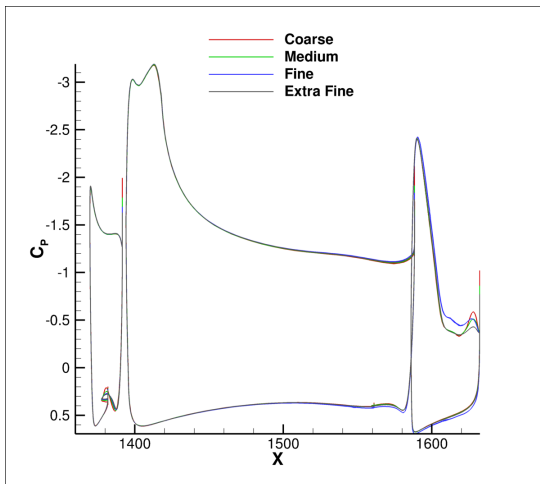
(b) $\eta = 0.151$ (LAVA)
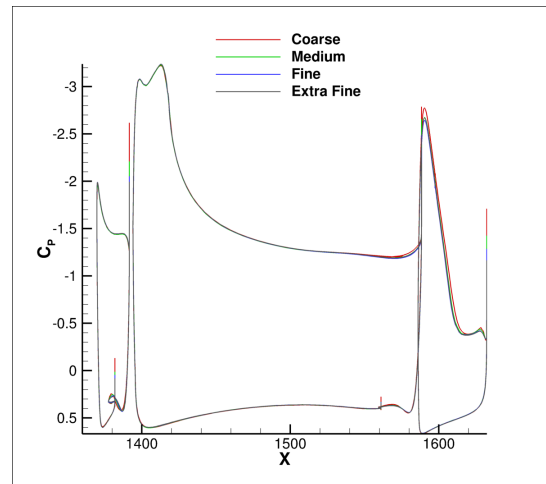
(c) $\eta = 0.552$ (OVERFLOW)
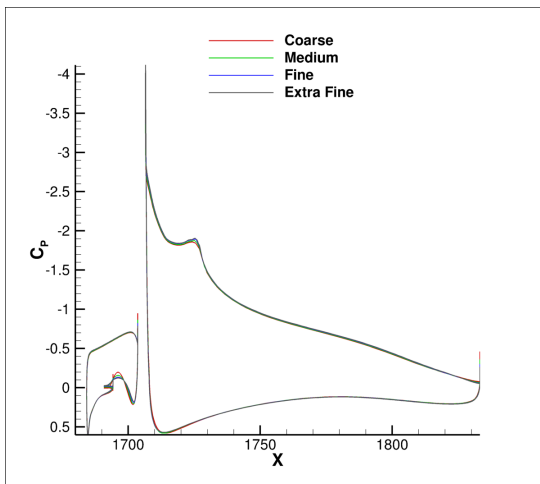
(d) $\eta = 0.552$ (LAVA)
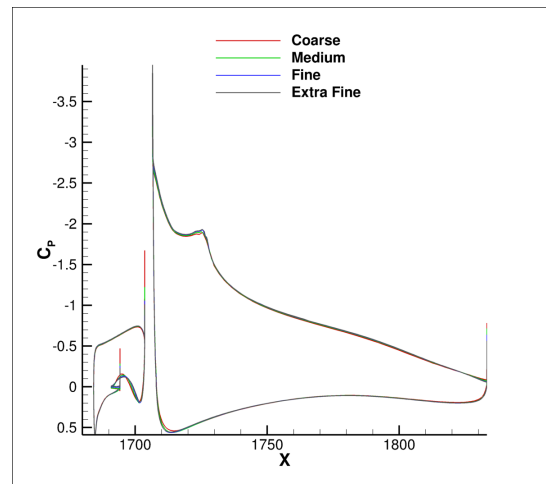
(e) $\eta = 0.908$ (OVERFLOW)

(f) $\eta = 0.908$ (LAVA)

Figure 8. Grid-refinement effects on $\alpha = 8°$ HL-CRM surface pressure distributions using OVERFLOW and LAVA.

11

American Institute of Aeronautics and Astronautics
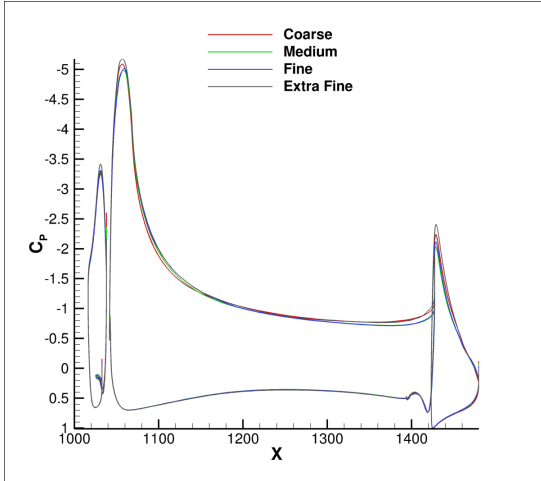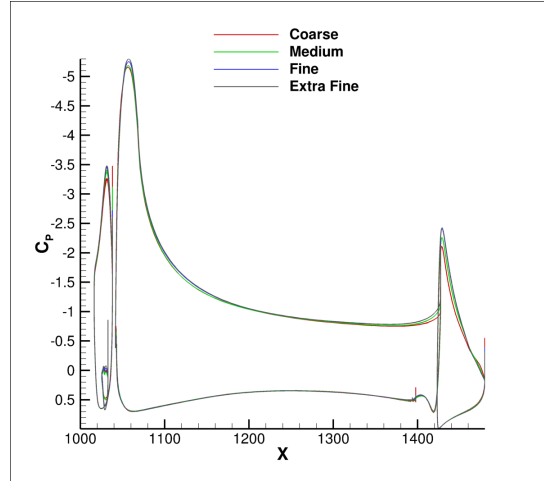
(a) $\eta = 0.151$ (OVERFLOW)

(b) $\eta = 0.151$ (LAVA)
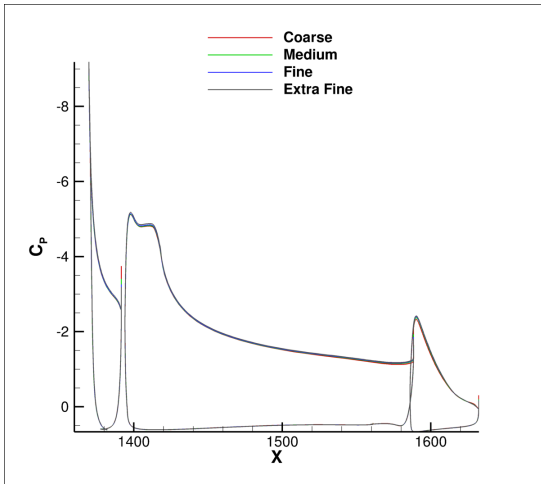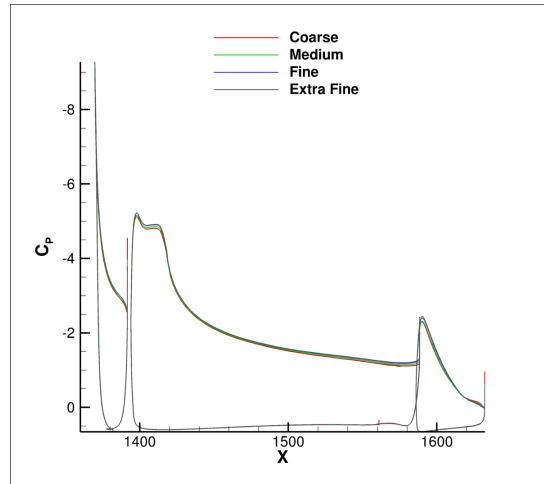
(c) $\eta = 0.552$ (OVERFLOW)

(d) $\eta = 0.552$ (LAVA)
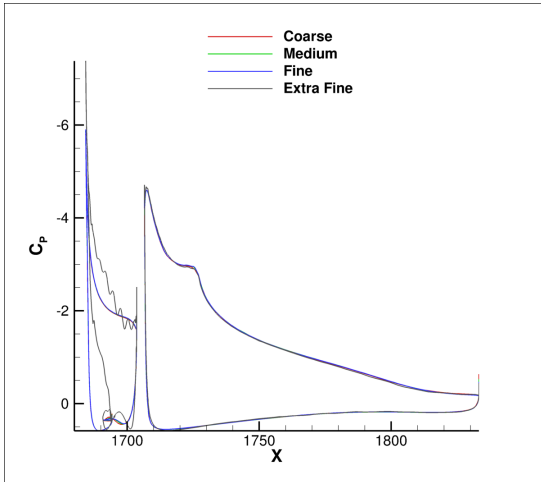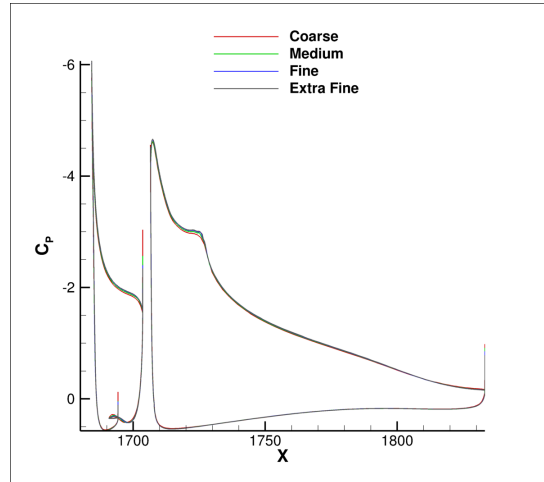
(e) $\eta = 0.908$ (OVERFLOW)

(f) $\eta = 0.908$ (LAVA)

Figure 9. Grid-refinement effects on $\alpha = 16°$ HL-CRM surface pressure distributions using OVERFLOW and LAVA.

12

American Institute of Aeronautics and Astronautics

4. Effect of Flap-Gap Seal (Case 1c)

Case1c was included in the workshop to assess the effect of sealing the flap gaps both on the grid generation and solution process. Figure 10 shows the effect on flow separation on the flap due to the seals using the SA-noft2-RC-QCR2000 model. The inboard portion of the inboard flap show a large separation, while the outboard portion of the inboard flap shows attached flow in contrast with the gap case. There is also a significant difference in the outboard flap separation line.
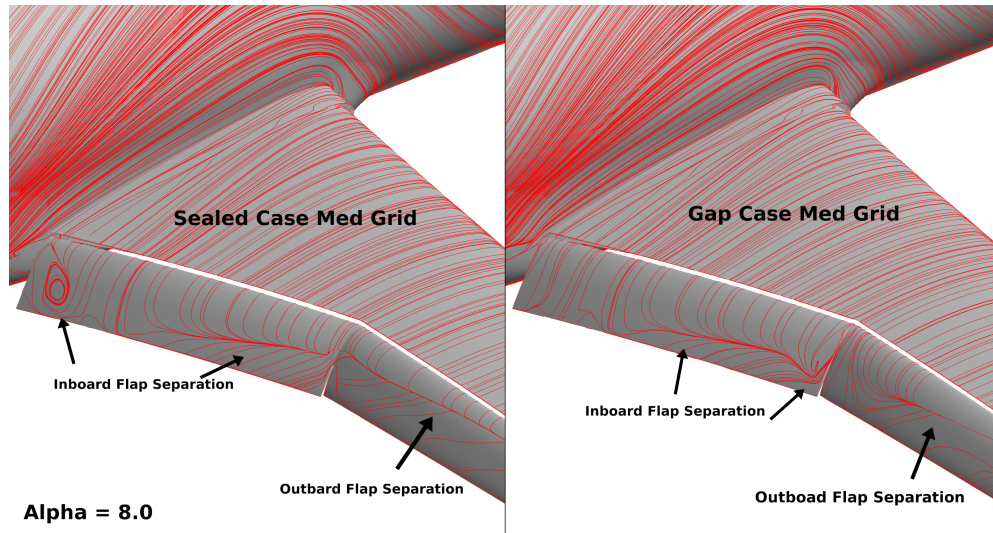
Figure 10. Effect of HL-CRM flap-gap seal on upper-surface flow patterns.

B. JSM

1. Nacelle/Pylon Off (Case 2a)

The force and moment coefficients predicted across the specified angle-of-attack range for the JSM with the nacelle/pylon off are shown in Fig. 11, and wing-surface pressure distributions for four spanwise locations are plotted in Fig. 12 for $\alpha = 4.36°$ and Fig. 13 for $\alpha = 18.58°$. The lift predictions show a strong influence from the specific simulation strategy used. For the baseline modeling approach (SA-noft2-RC-QCR2000, non-time-accurate), a stalling behavior is predicted to occur prematurely relative to experiment after an angle of attack of 14.54° in both the OVERFLOW and LAVA solutions. Below this angle, however, reasonable agreement with the experiment was obtained. The substantial decrease in lift relative to experiment for higher angles of attack is attributed to excessive mid-span separation that was predicted, as can be inferred from Fig. 13b. It was subsequently recognized that this may be influenced by the fact that the solutions were initialized using a "cold start" from free-stream conditions. An additional alpha sweep with the baseline modeling was performed using "warm starts" in which solutions were initialized with converged solutions from the next lower angle of attack. This had the effect of producing a high-lift solution branch, although there is still some premature stall. The difference in behavior between cold and warm starts has important implications on the simulation of high-lift systems. For an actual aircraft, higher angles of attack or attained by first passing through lower angles of attack. On the other hand, it is generally desirable to be able to run the CFD 'blindly' for a given angle of attack without knowledge of solution behavior at different angles.

Variations of the modeling strategy each had notable impacts on the results. Without QCR, the lift-curve maintains a high-lift branch, but both the stall angle of attack and maximum-lift coefficient are overpredicted. When time-accurate simulation is used (with QCR), however, the lift curve switches to a high-lift branch even for cold starts. There is still premature stall, but it is less extreme than the non-time-accurate solution and better follows the experimental lift curve pre-stall. Including laminar-turbulent transition had an overall positive effect on the predictions. Both cold starts and warm starts were attempted, non-time-accurately, with transition modeling. Similar to the fully turbulent simulations, transitional cold starts (not included here) showed premature stall, while the warm starts followed a higher-lift branch. Compared to the fully turbulent warm starts, these data showed better lift agreement with experiment, especially at lower angles of attack, but maximum lift was overpredicted. However, this observation only applies for QCR being used.

13

American Institute of Aeronautics and Astronautics

The pitching-moment coefficient was predicted to be more positive than was measured for the majority of solutions. The exception to this are the transitional solutions at $\alpha = 14.54°$ and $18.58°$, which agree much better with experiment for pitching-moment coefficient; however, the discrepancies in lift indicate that this agreement may be superfluous. For the drag coefficient, all models overpredict it for all angles of attack, with the two warm starts (fully turbulent and transitional) agreeing better at higher angles of attack. This is most likely a result of the high-lift branch featuring much reduced separation than the low-lift branch.
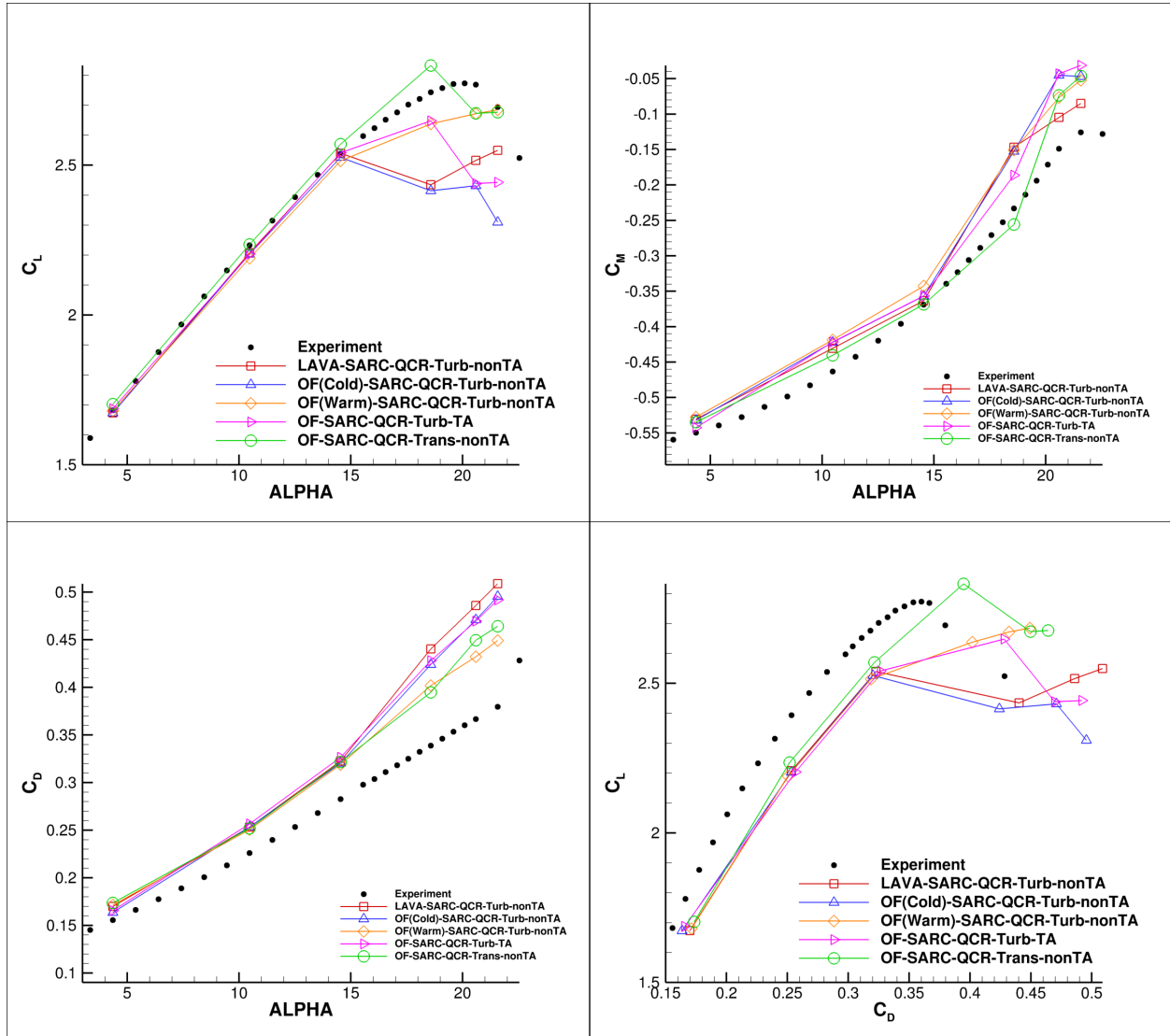
Figure 11. Force and moment coefficients for the JSM with nacelle/pylon off.

14

American Institute of Aeronautics and Astronautics
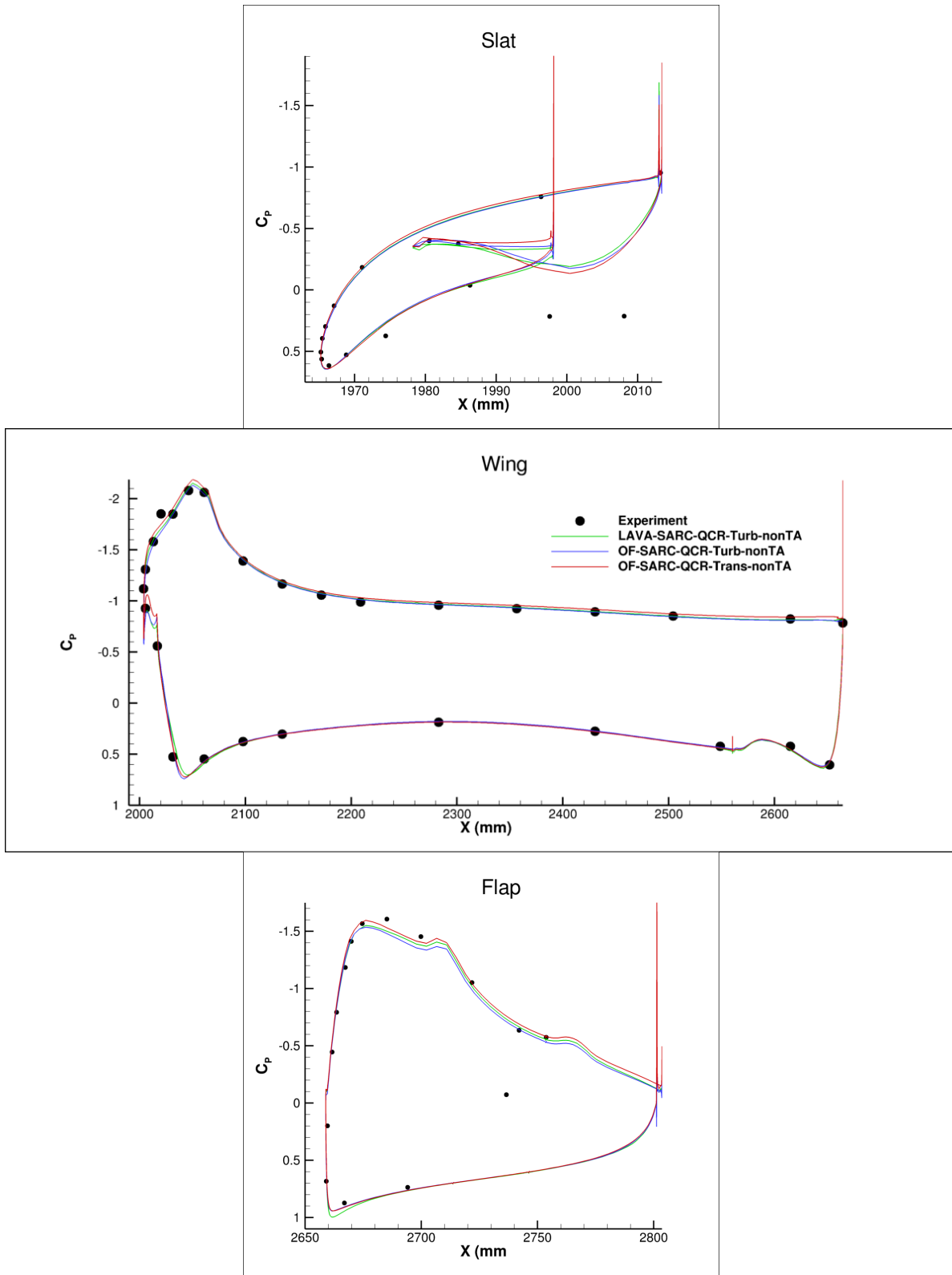
Figure 12. Wing surface pressure distributions for the JSM with nacelle/pylon off at $\alpha = 4.36°$.

American Institute of Aeronautics and Astronautics

Slat

Wing

Flap
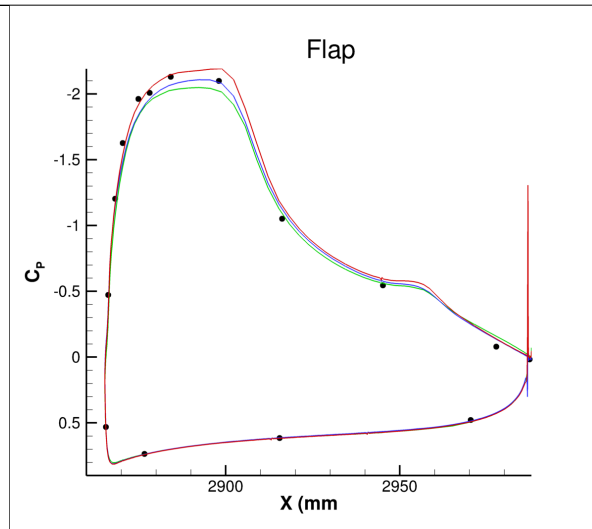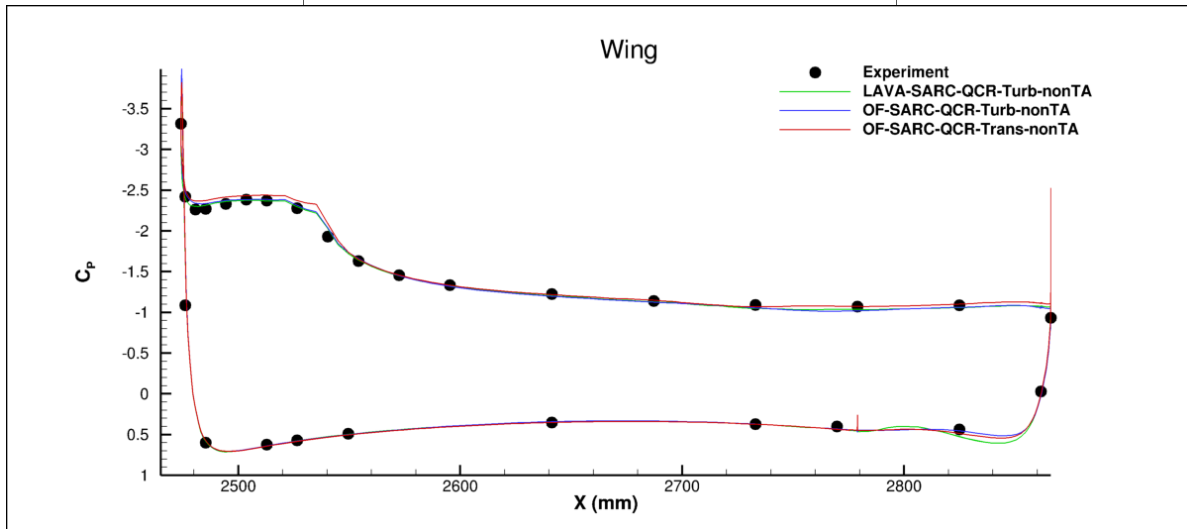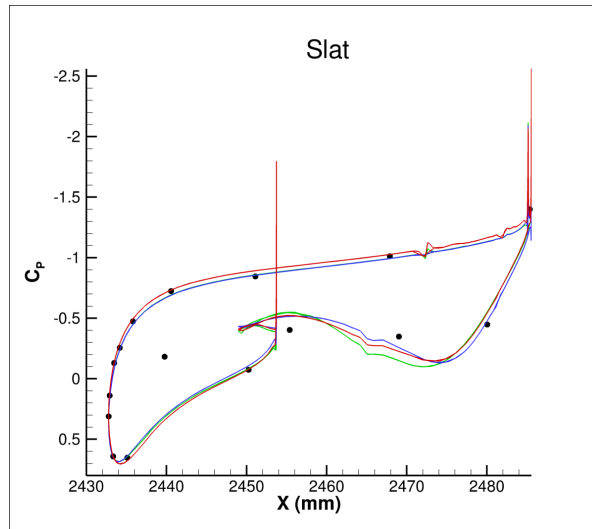
(b) Section E-E ($\eta = 0.56$)

Figure 12. (Continued).

16

Slat

Wing

Flap
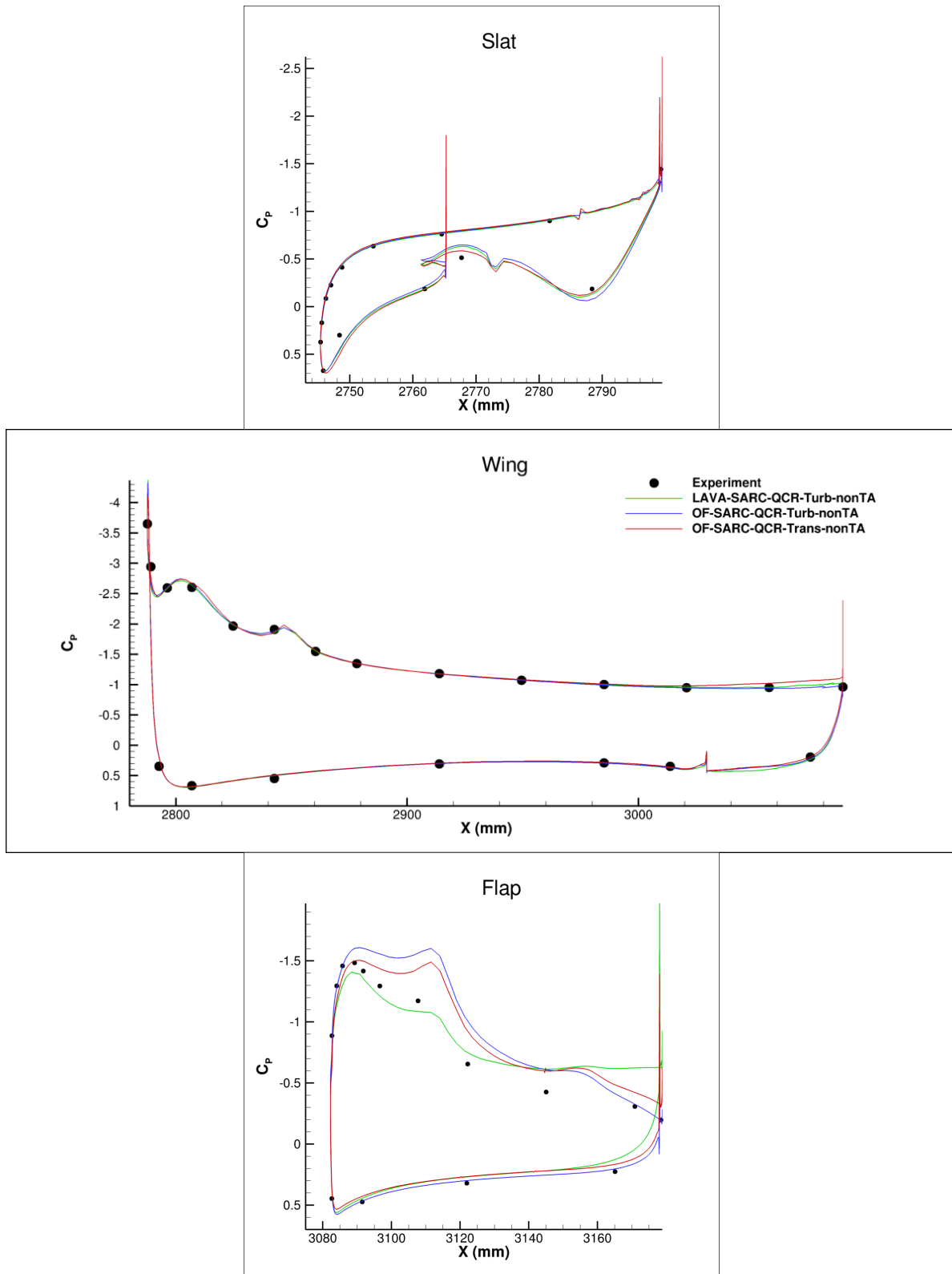
(c)   Section G-G ($\eta = 0.77$)

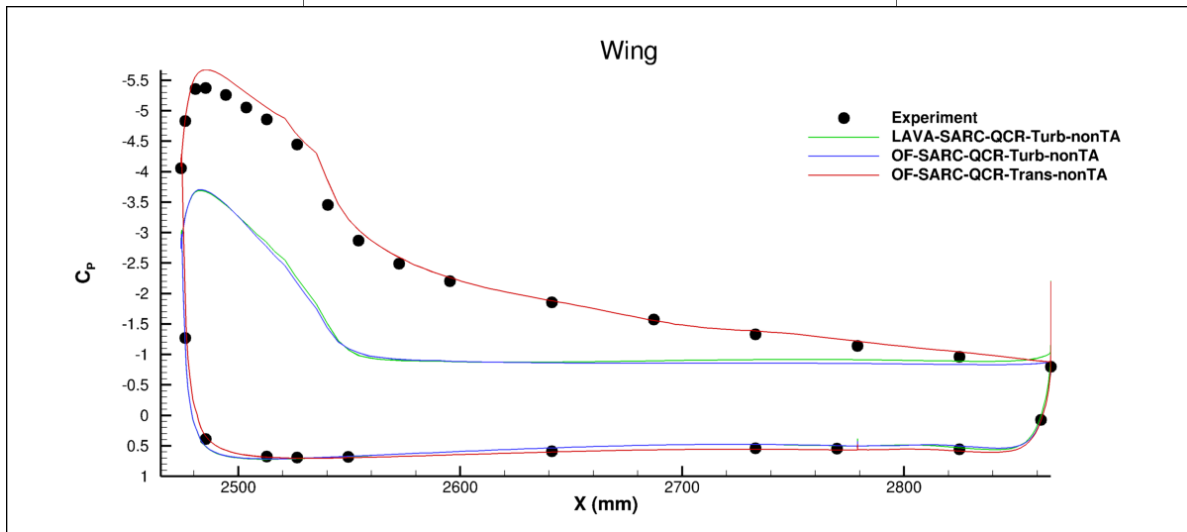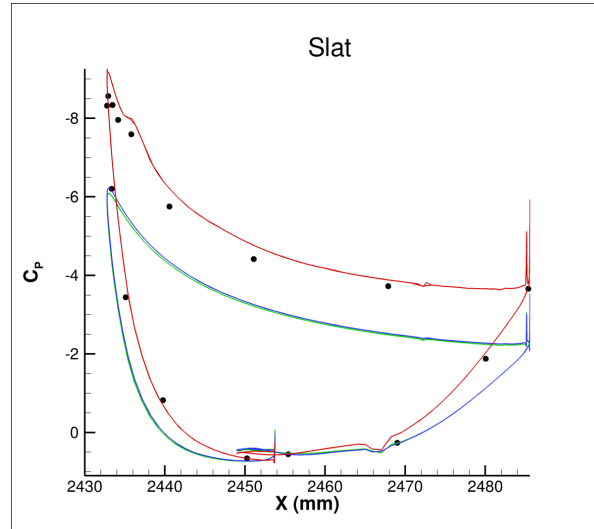**Figure 12. (Continued).**

American Institute of Aeronautics and Astronautics
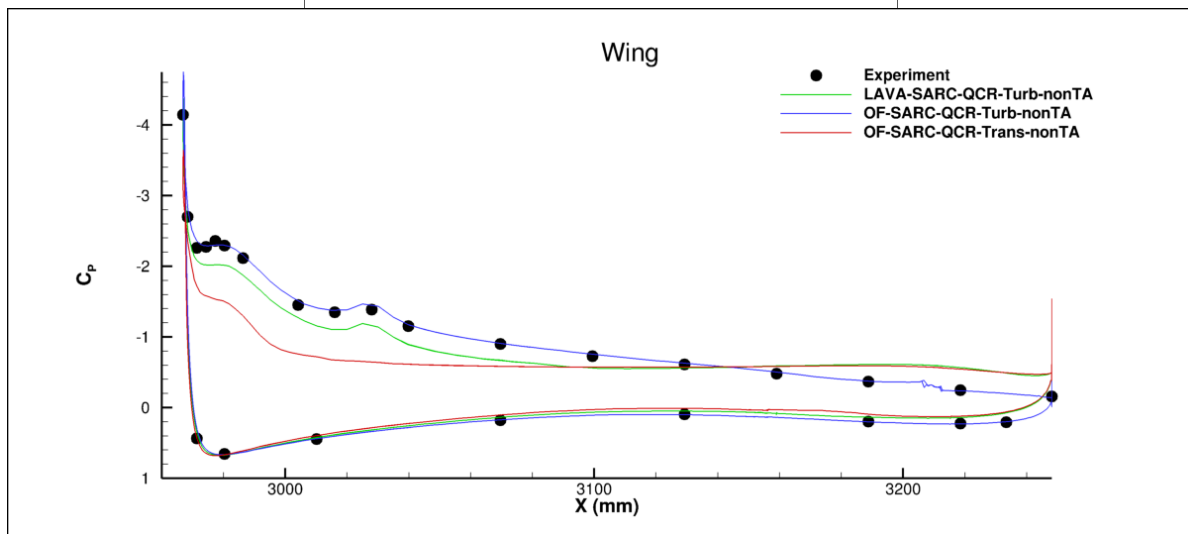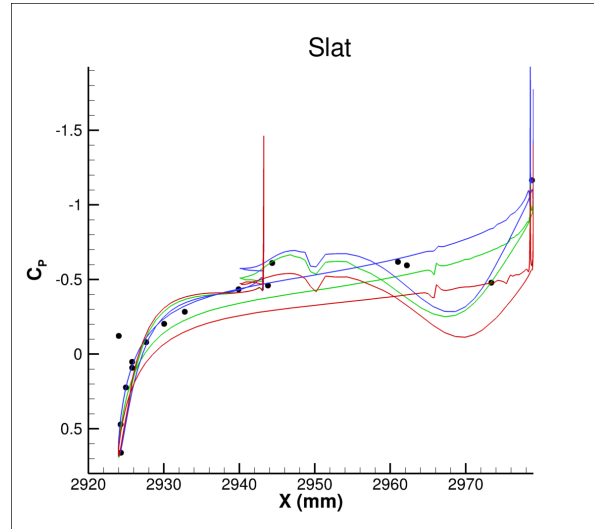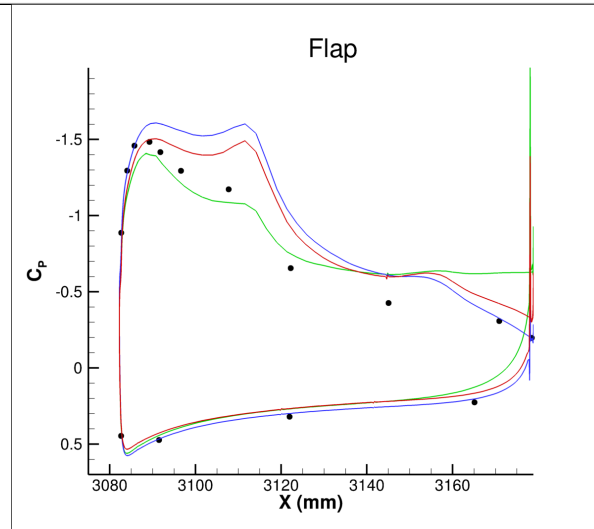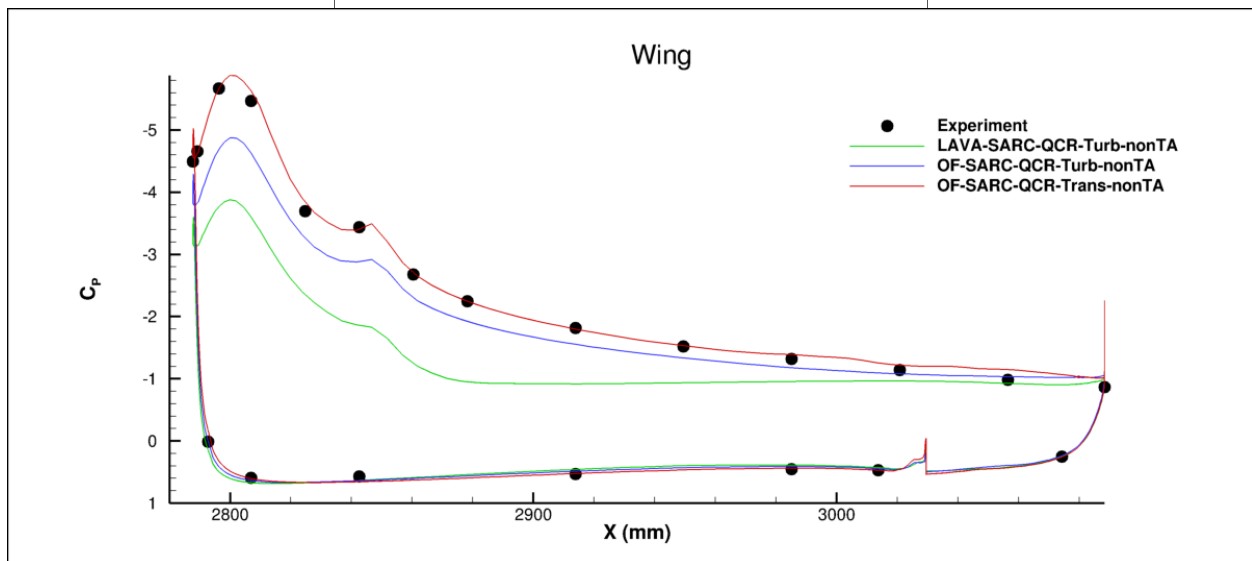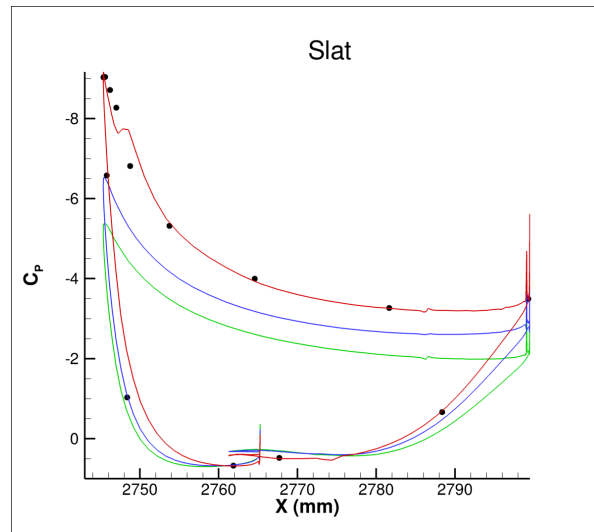
(d)   Section H-H ($\eta = 0.89$)

Figure 12. (Concluded).

American Institute of Aeronautics and Astronautics

Slat

Wing

Flap
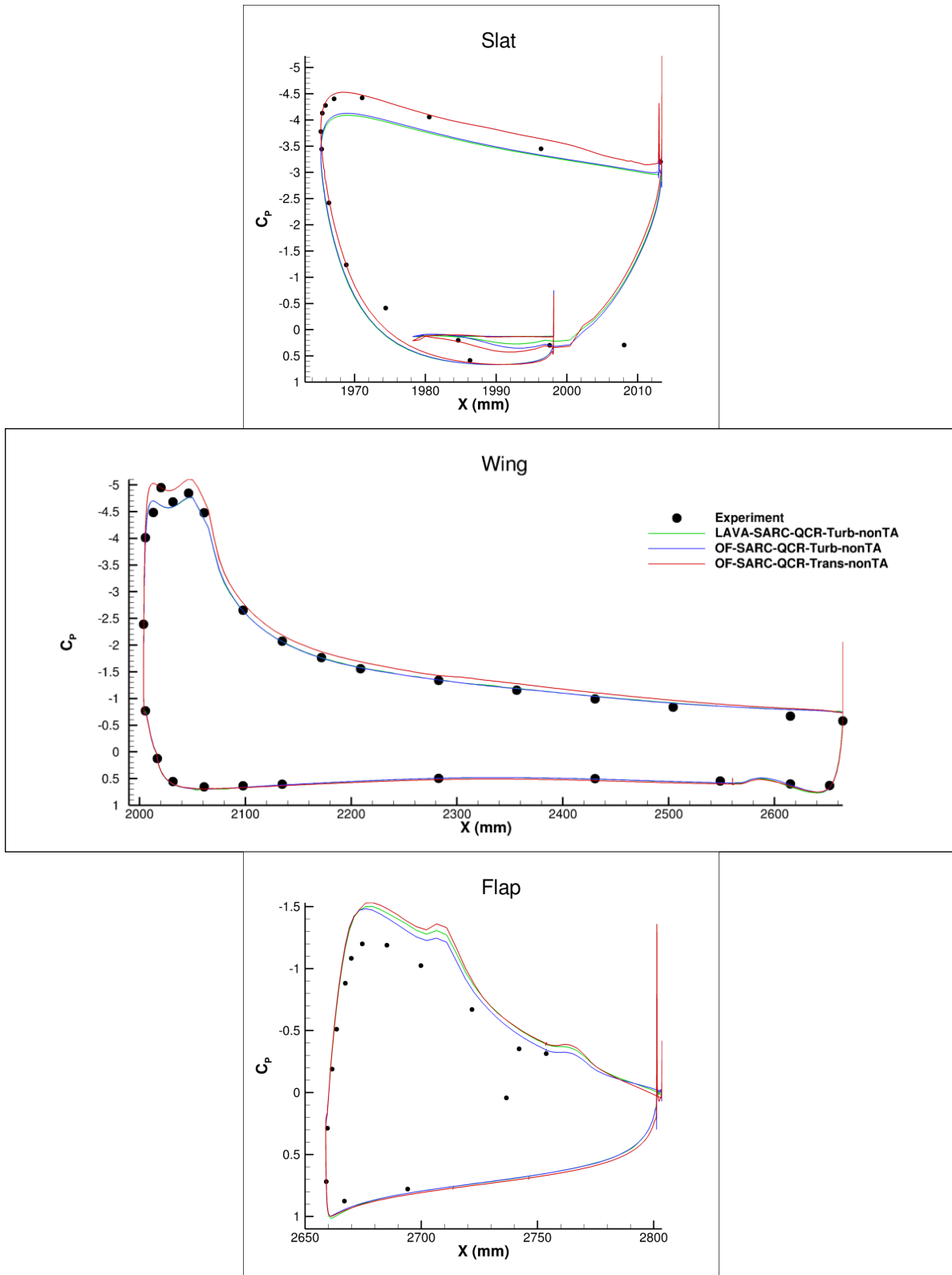
(a)   Section B-B (η = 0.25)

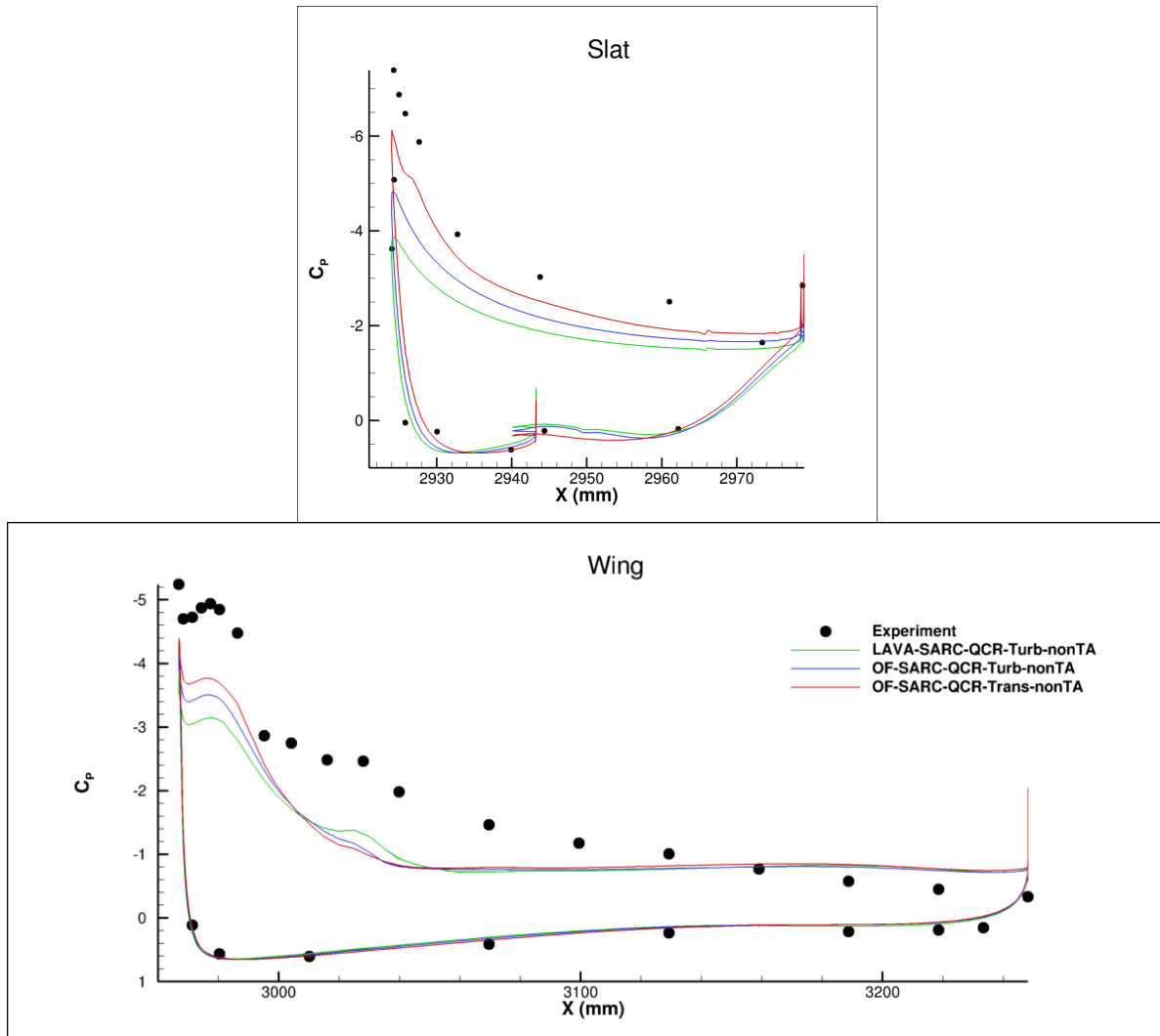**Figure 13. Wing surface pressure distributions for the JSM with nacelle/pylon off at α = 18.58°.**

American Institute of Aeronautics and Astronautics
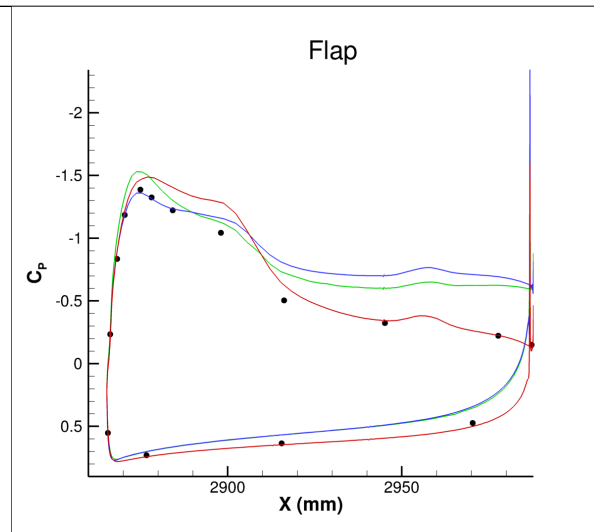
(b) Section E-E ($\eta = 0.56$)

Figure 13. (Continued).

American Institute of Aeronautics and Astronautics

Slat

Wing

Flap

(c)   Section G-G (η = 0.77)

Figure 13. (Continued).

American Institute of Aeronautics and Astronautics

(d) Section G-G (η = 0.89)

Figure 13. (Concluded).

2. Nacelle/Pylon On (Case 2c)

The predicted force and moment coefficients for the nacelle/pylon on are shown in Fig. 14, and wing-surface pressure distributions for four spanwise (the same as for Case 2a) locations are plotted in Fig. 15 for α = 4.36° and Fig. 16 for α = 18.58°. Note that there was no observed effect of cold versus warm starts on the converged solutions, so no distinction is made in the Case 2c results. Unlike for the nacelle/pylon off case, running without QCR leads to a significantly premature stalling behavior. The lift curve leaves the linear regime sharply after 10.47° angle of attack, and increases more slowly than either the experiment or the solutions that included QCR.

Time accuracy had a less significant impact with the nacelle/pylon on, as both the time-accurate and non-time-accurate predictions agree well with each until through stall. After stall, the lift coefficient of the non-time-accurate solution drops off rapidly, whereas the time-accurate solutions exhibited a softer stall character that is more consistent with experiment. When taken in context with the nacelle/pylon-off solution behavior, other participants' data presented at HiLiftPW-3, and the relevant flow physics, some inferences may be drawn. First, the nacelle/pylon-on configuration does not exhibit the likelihood of multiple solutions in the pre-stall regime as was observed with the nacelle/pylon off. The presence of the nacelle and pylon seems to automatically 'select' which flow-separation behavior will prevail in the solution, regardless of starting from free-stream or from a lower angle of attack. Second, time accuracy improves the post-stall prediction, seemingly due to the large amounts of separation prevalent in the

American Institute of Aeronautics and Astronautics

solution. For shedding events, local time stepping causes non-physical advection of vortices, skewing the force and moment history, whereas time accuracy ensures that the shedding is globally consistent and retains more physicality.

Including transition modeling had a favorable impact for the nacelle/pylon-on case on the agreement between CFD and experiment. For the lift curve, the transitional prediction agrees much more closely with experiment than fully turbulent, including for lower angles of attack, and shows very strong agreement until stall. Around stall, the requested data for HiLiftPW-3 did not include the exact maximum-lift angle of attack from the experiment. At the immediate lower angle (18.58°), the transitional prediction agrees well, but at the next higher angle (20.59°), which is post-stall, the transitional CFD underpredicts the lift in a manner consistent with fully turbulent results. It must be noted, however, that the angles of attack requested for HiLiftPW-3 provide a relatively coarse resolution of the lift curve near stall, and it is possible that additional angles of attack may improve the perceived agreement. The drag and pitching-moment predictions also show better agreement with experiment than those obtained fully turbulent, especially at higher angles of attack; however, noticeable discrepancies remain. The impact of transition modeling in the solution was also evident in the surface pressure distributions. For example, the data for an angle of attack of 18.58° plotted in Fig. 16 shows closer agreement between transitional CFD and experiment than fully turbulent CFD an experiment. This includes more accurately capturing the suction peaks at $\eta = 0.25$ (Fig. 16a) and predicting the correct, attached-flow behavior at $\eta = 0.77$ (Fig. 16c). More outboard at $\eta = 0.89$ (Fig. 16d), however, all methods considered show main-element flow separation in disagreement with the experiment.

Surface contours of the vorticity magnitude for $\alpha = 18.58°$ are shown in Fig. 17 for LAVA and OVERFLOW (non-time-accurate) and compared with the corresponding surface oil flow image from the experiment [8]. In this, the bulk flow patterns can be observed, including regions of separation, which are identifiable in the CFD images as wedges of low vorticity magnitude, and laminar-turbulent transition. Both OVERFLOW solutions show a single separation wedge on the main element behind the outboard-most slat bracket. This is consistent with the experiment; however, the size of the separation wedge is consistently overpredicted. With LAVA, an additional separation wedge is present at the next inboard slat bracket, but this is not present in the oil flow. In the transitional solution, regions of low surface vorticity near the main-element leading edge coincide with laminar separation bubbles, and similar flow patterns are visible in the oil flow.

A further assessment of the laminar-turbulent transition prediction used in the CFD was made by comparing transition patterns. In the experiment, transition was visualized using China clay [7], and pictures of the surface patterns are available [8]. To provide a meaningful equivalent from the CFD, Spalart's Turbulent Index [19] was employed as a surface sensor to detect whether or not the boundary layer is turbulent. Images of the experimental [7] and computational transition patterns are included as Figs. 18, 19, and 20 for angles of attack of 4.36°, 10.47°, and 18.58°, respectively. Strong qualitative agreement between the China clay and the predicted transition patterns were observed across the angle-of-attack range.
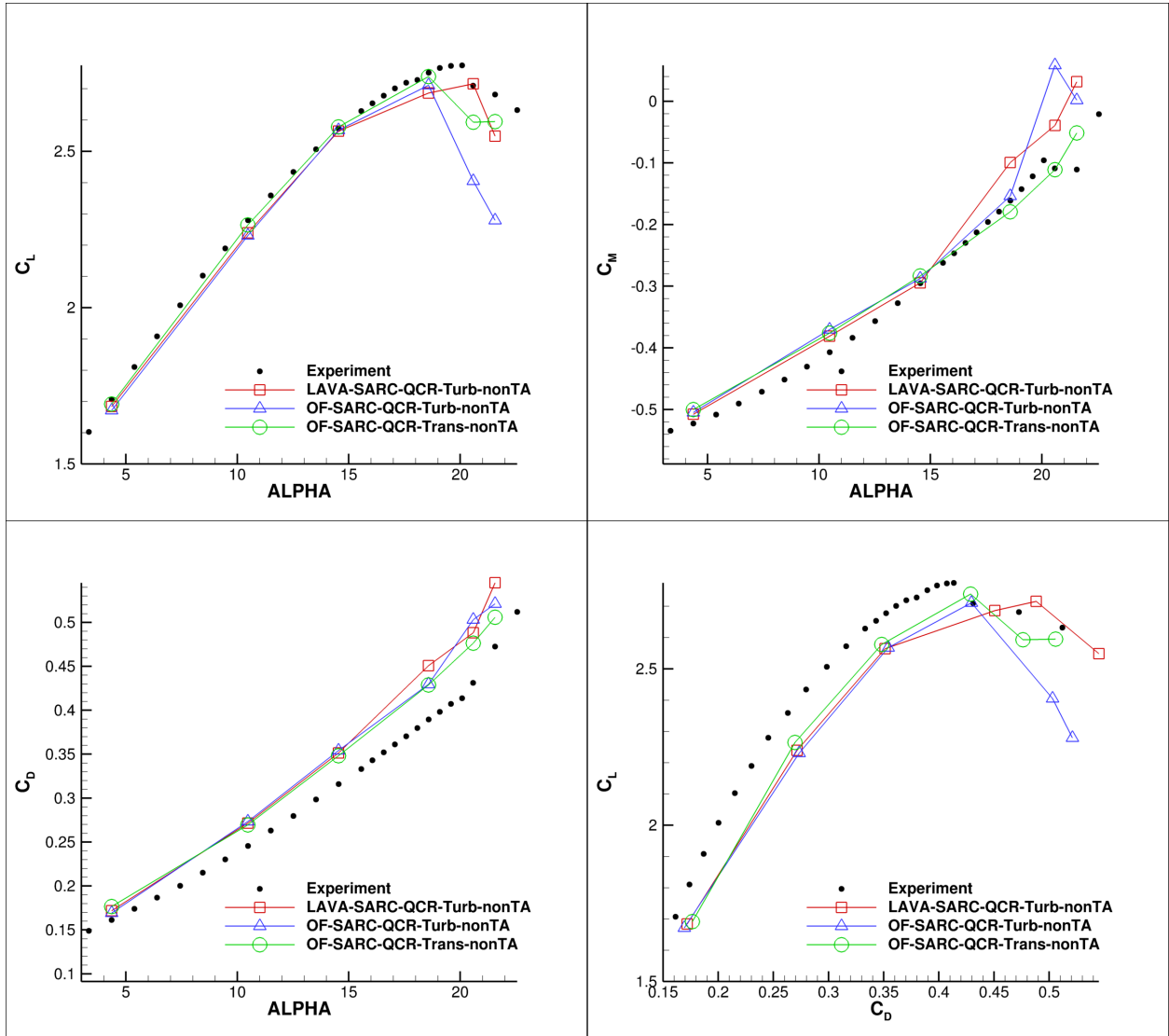
American Institute of Aeronautics and Astronautics

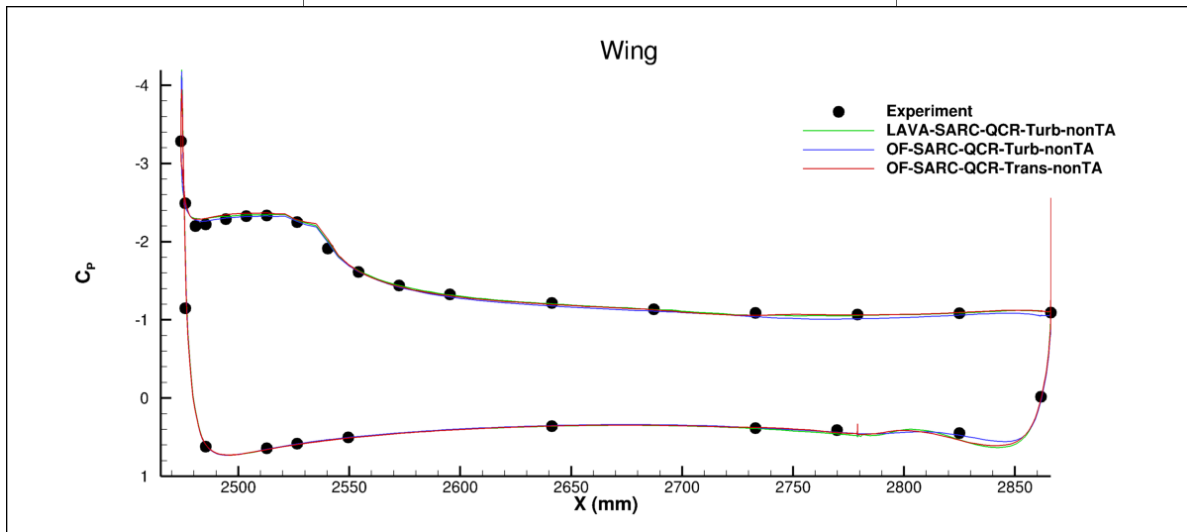**Figure 14. Force and moment coefficients for the JSM with nacelle/pylon off.**
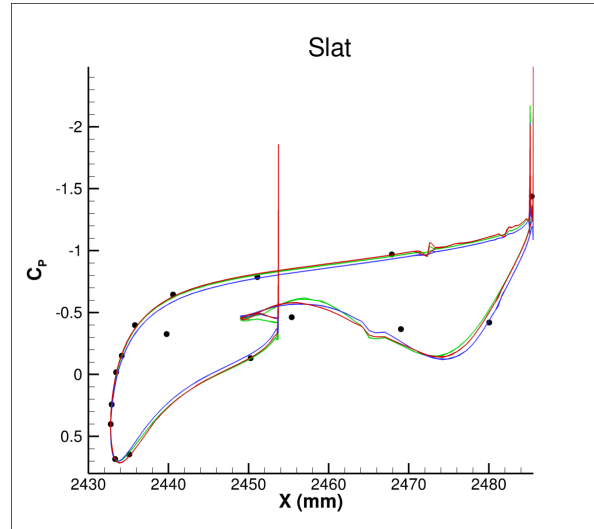
American Institute of Aeronautics and Astronautics
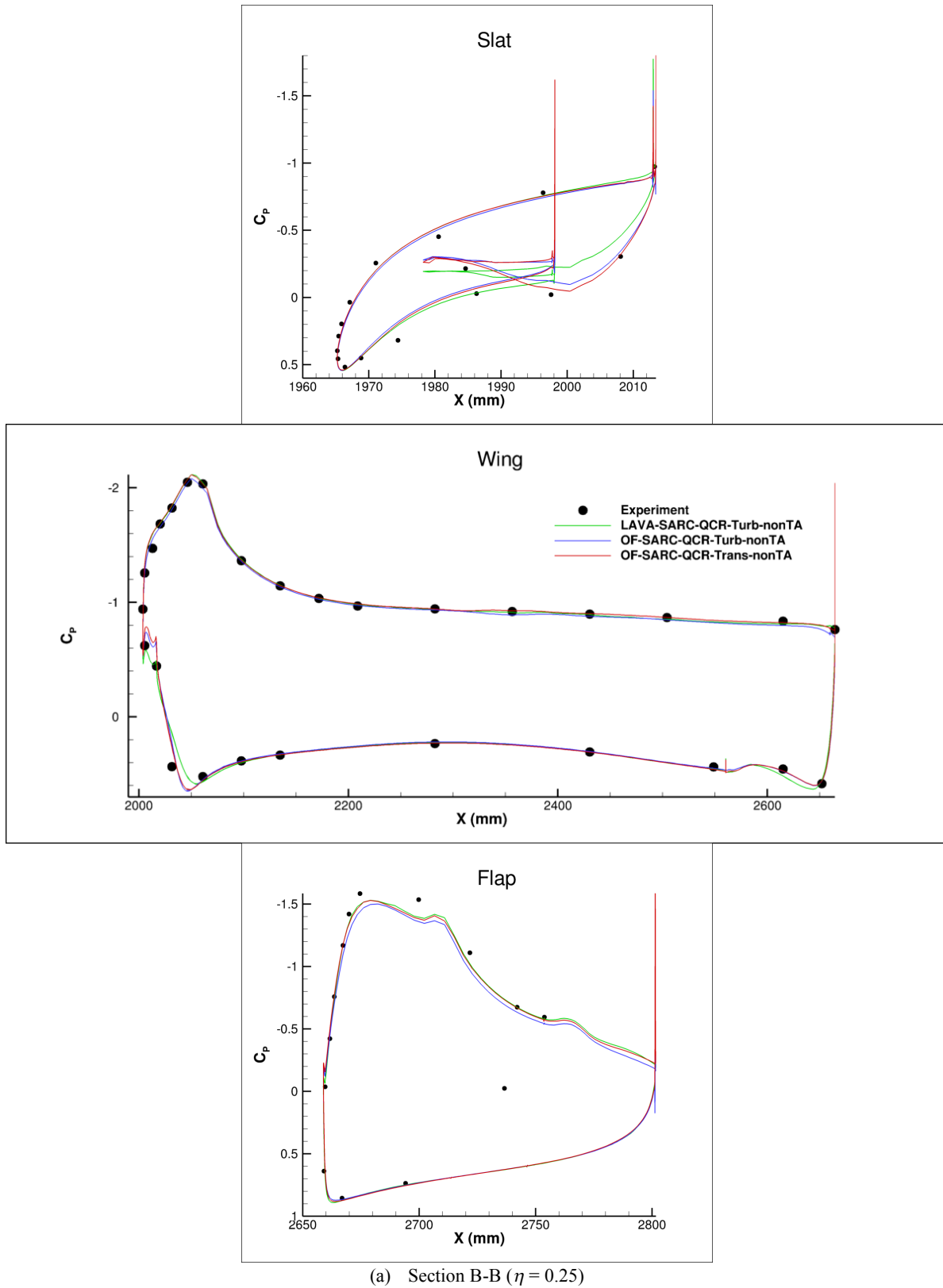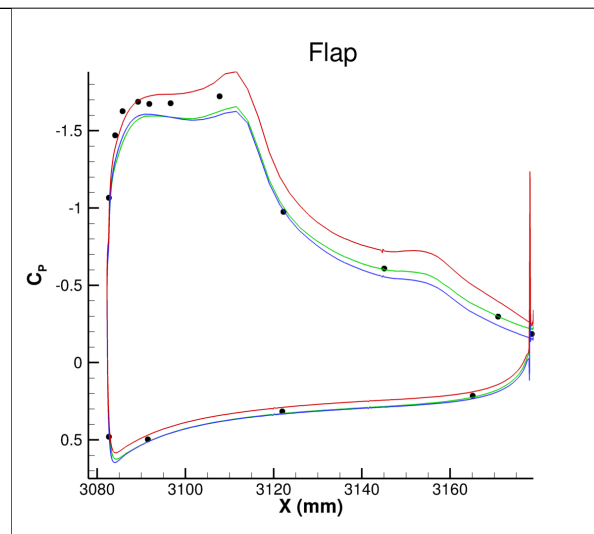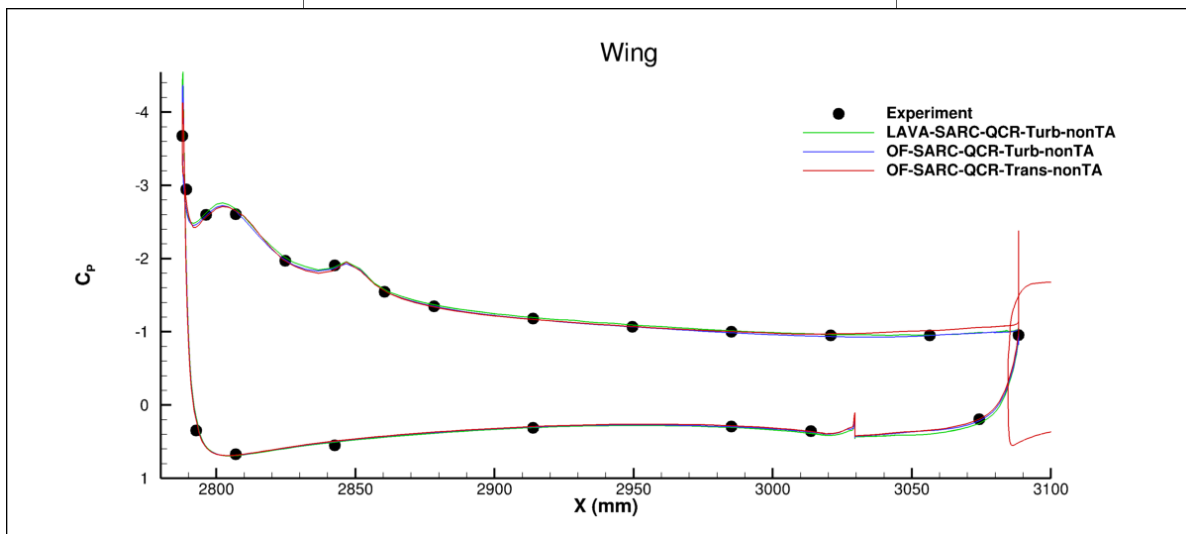
Figure 15. Wing surface pressure distributions for the JSM with nacelle/pylon on at α = 4.36°.

American Institute of Aeronautics and Astronautics
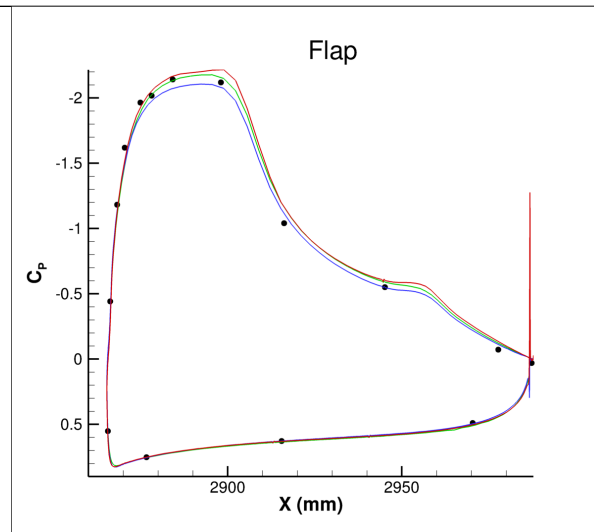
(b)   Section E-E ($\eta = 0.56$)

Figure 15. (Continued).

Slat

Wing

Flap

(c)   Section G-G (η = 0.77)

Figure 15. (Continued).

American Institute of Aeronautics and Astronautics
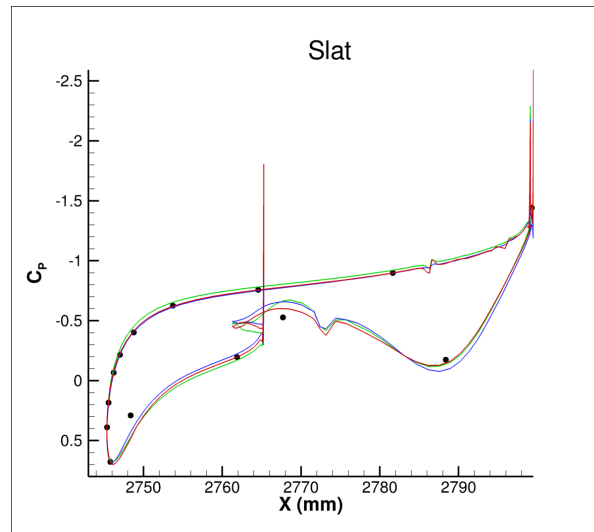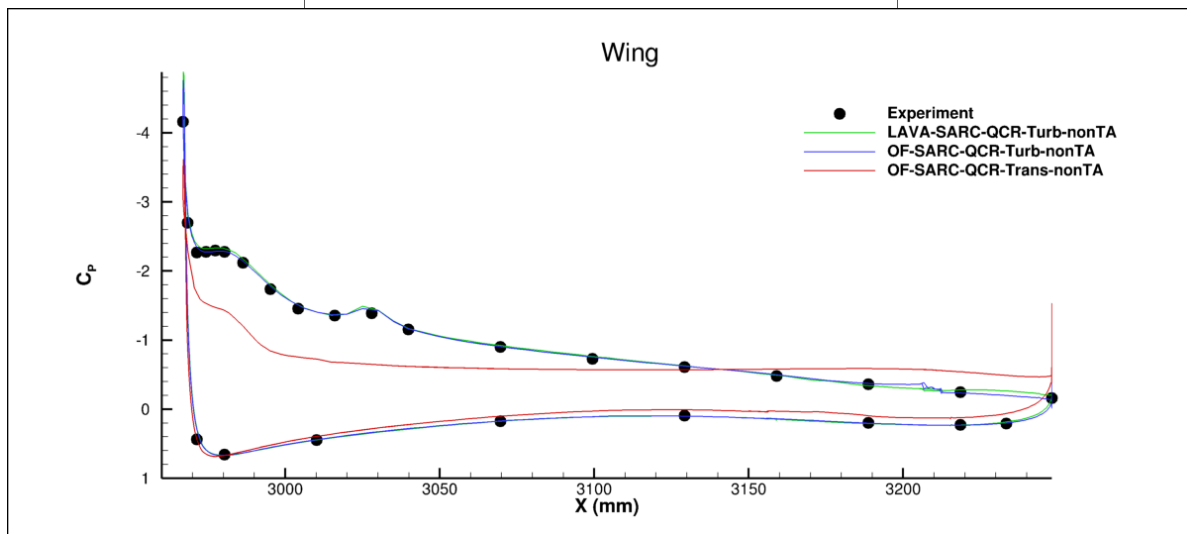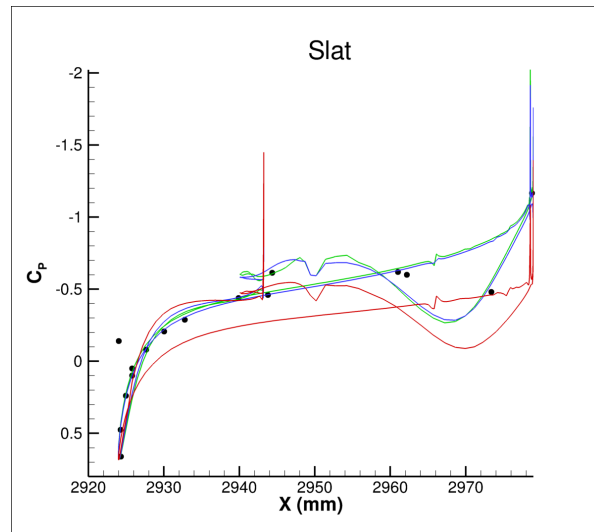
(d)   Section H-H ($\eta = 0.89$)

Figure 15. (Concluded).

American Institute of Aeronautics and Astronautics

(a)   Section B-B (η = 0.25)
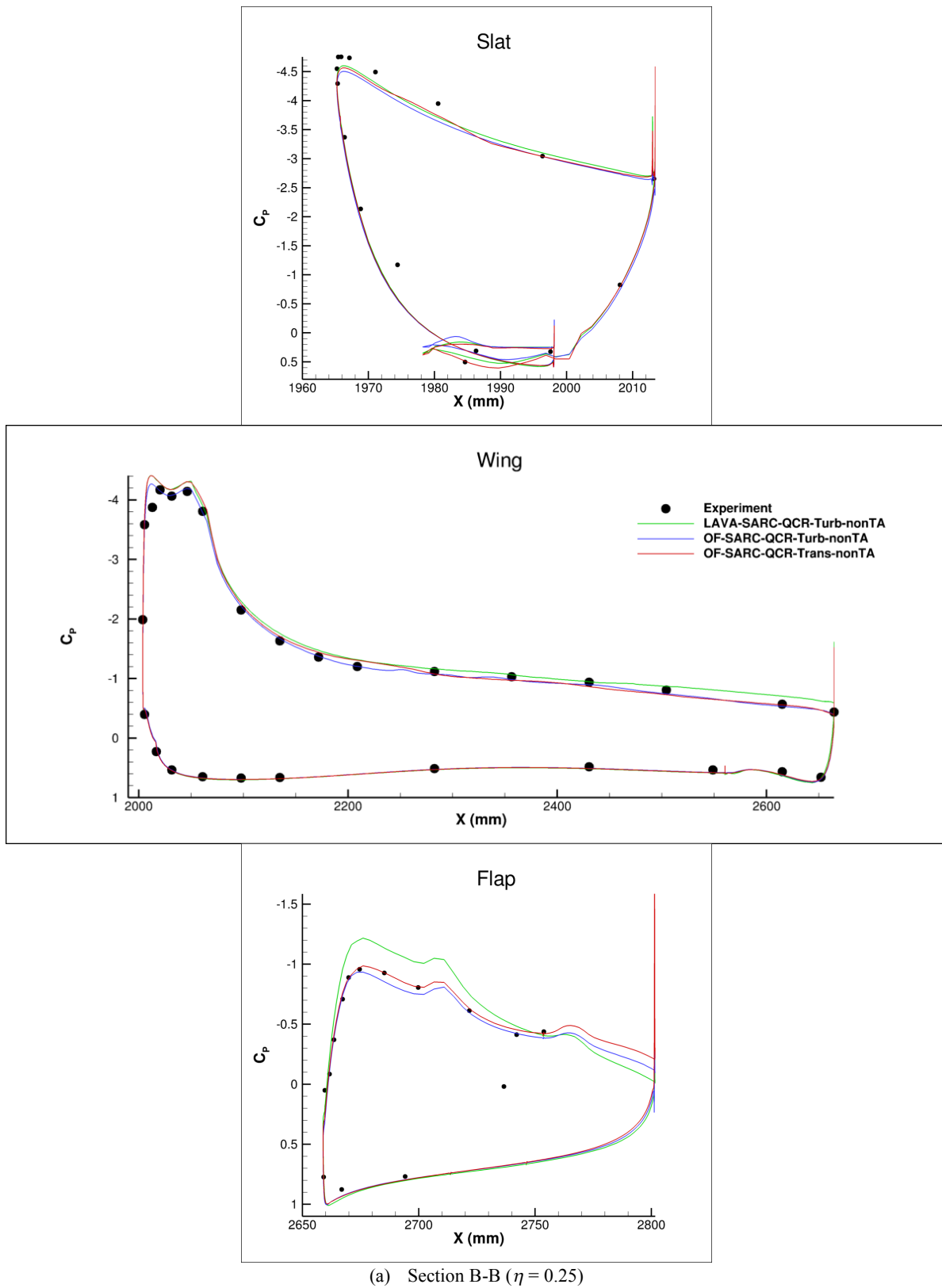
Figure 16. Wing surface pressure distributions for the JSM with nacelle/pylon on at α = 18.58°.
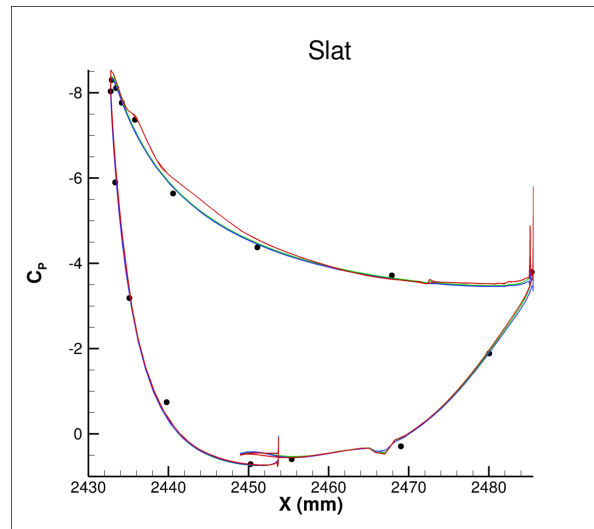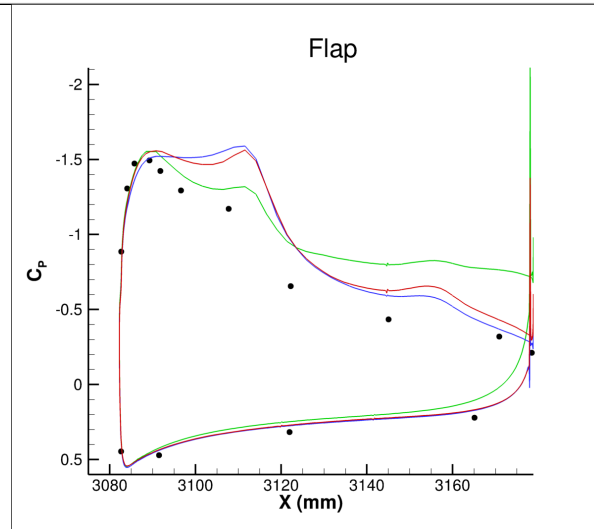
American Institute of Aeronautics and Astronautics

Slat

Wing

Experiment
LAVA-SARC-QCR-Turb-nonTA
OF-SARC-QCR-Turb-nonTA
OF-SARC-QCR-Trans-nonTA

Flap
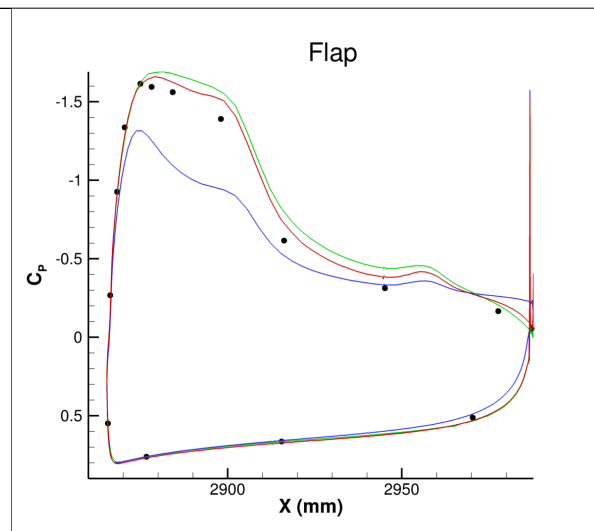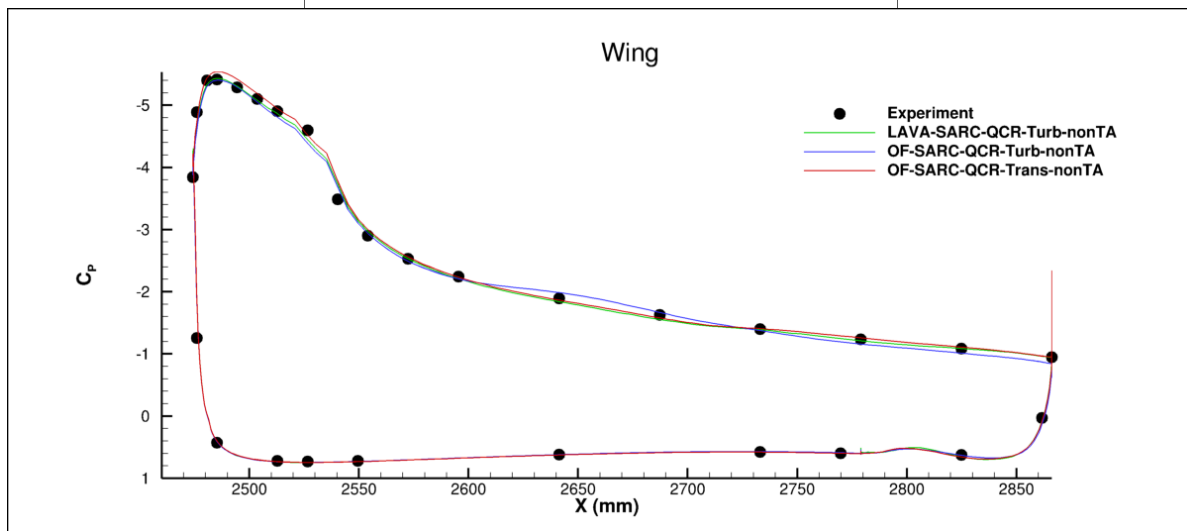
(b)   Section E-E ($\eta = 0.56$)

Figure 16. (Continued).

American Institute of Aeronautics and Astronautics

Slat

Wing

Flap

(c) Section G-G (η = 0.77)

Figure 16. (Continued).

31

American Institute of Aeronautics and Astronautics
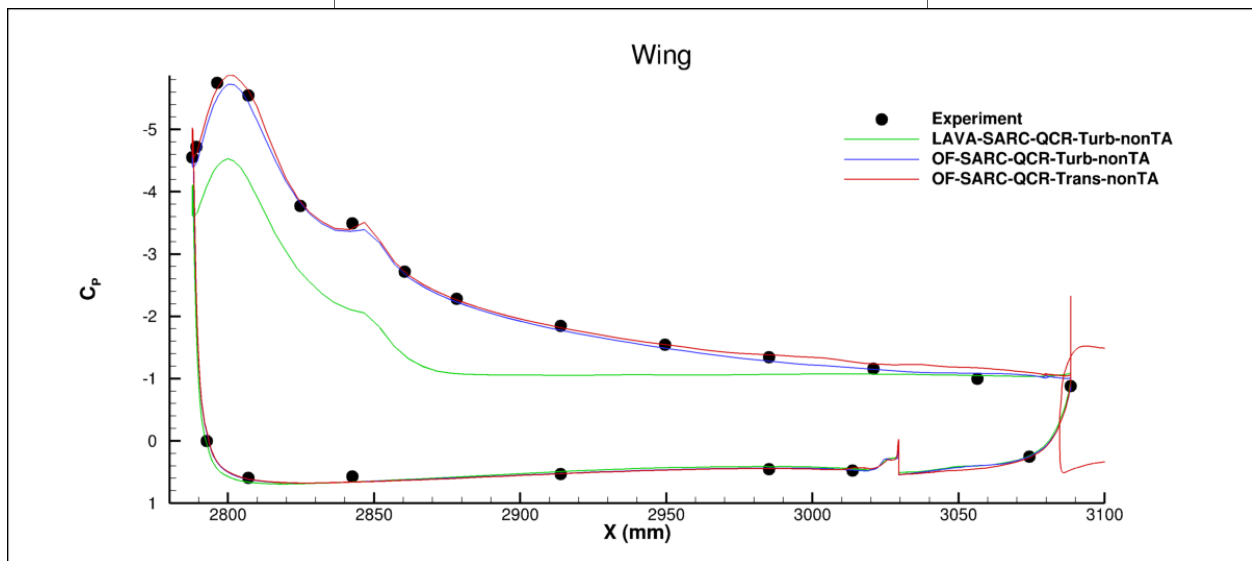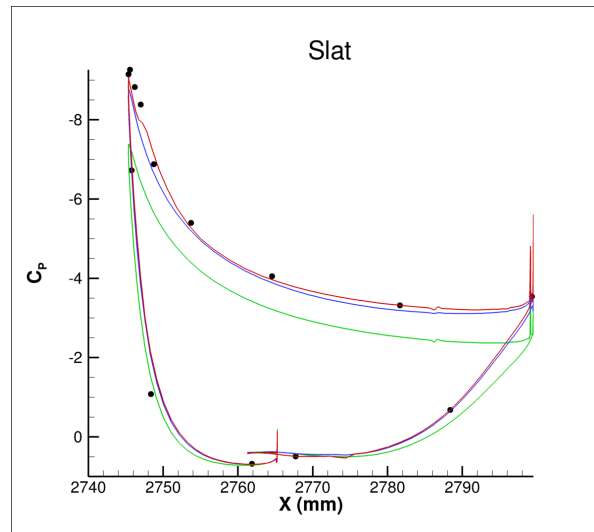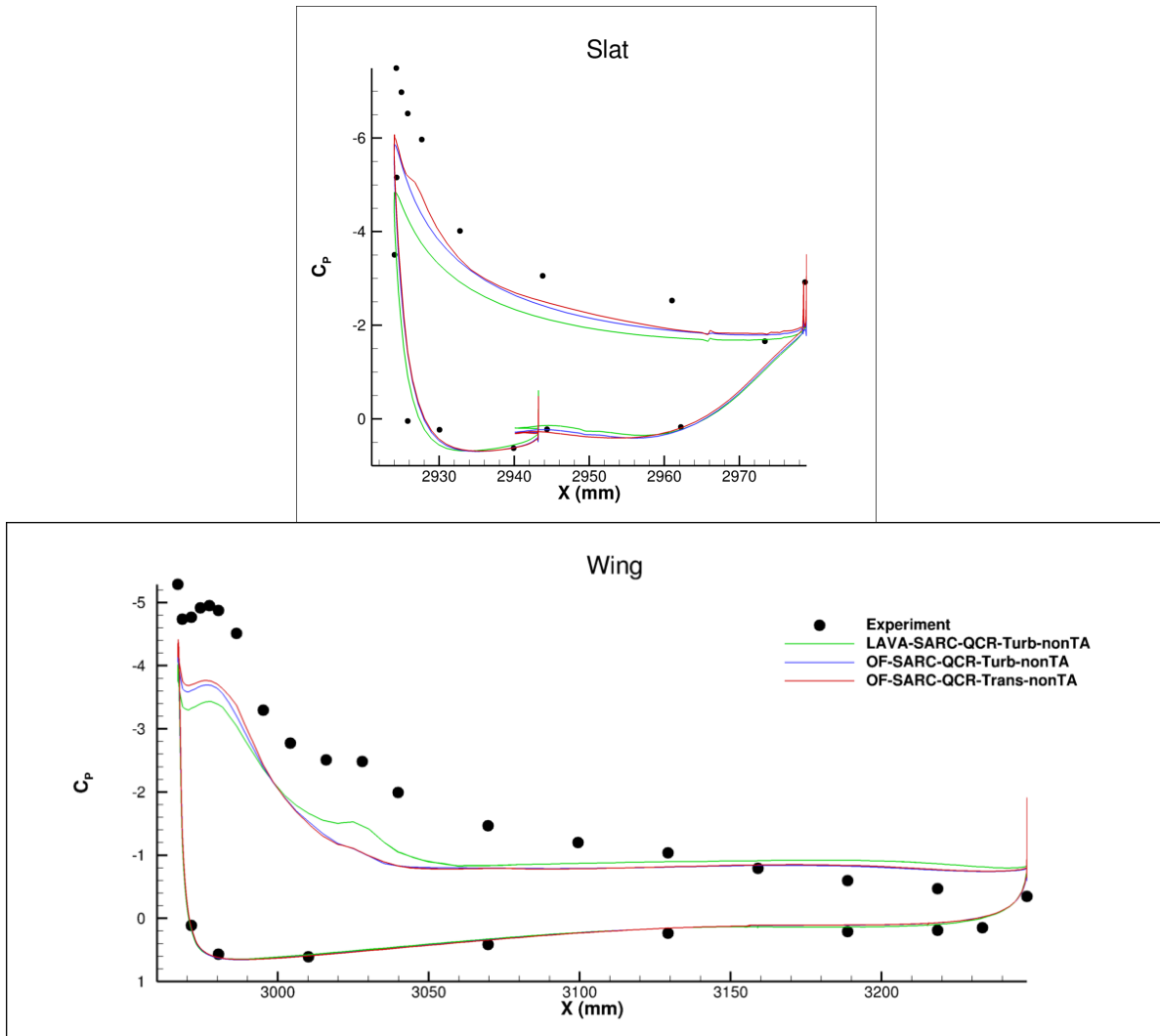
(d)   Section H-H ($\eta = 0.89$)

Figure 16. (Concluded).

American Institute of Aeronautics and Astronautics
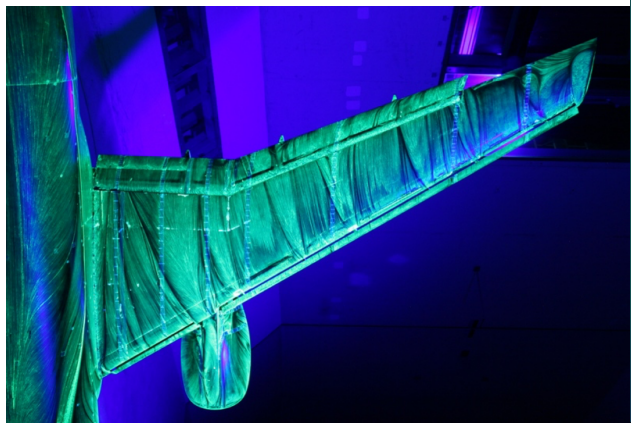
(a) Experiment [8]
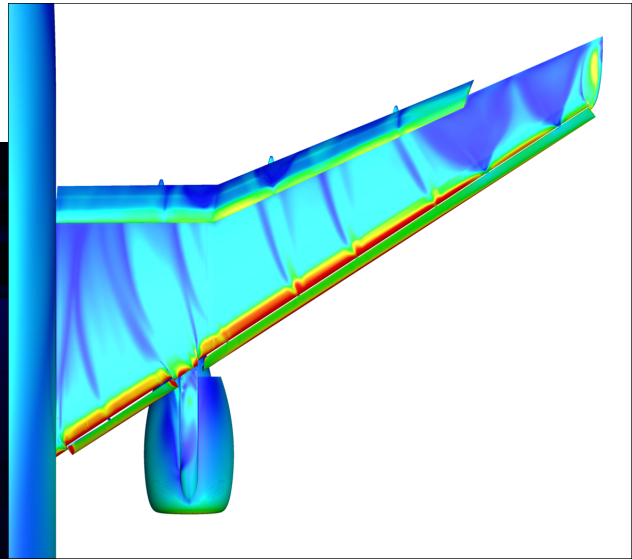
(b) LAVA
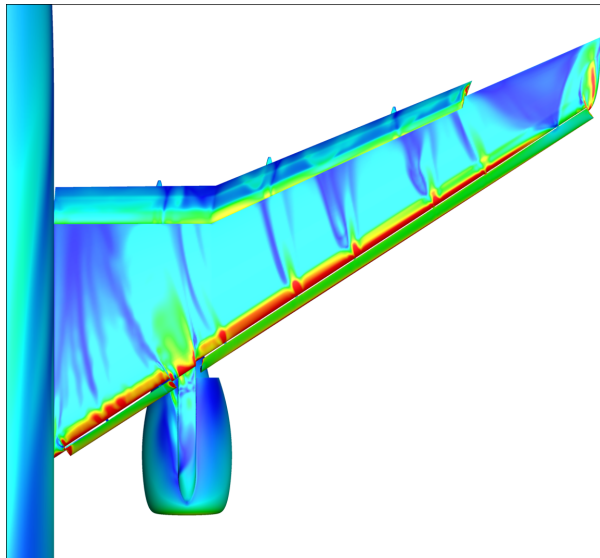
(c) OVERLFOW (turbulent)
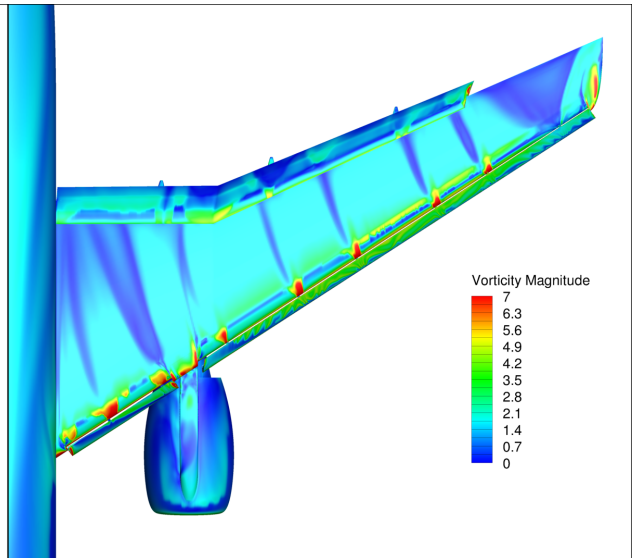
(d) OVERFLOW (transitional)

Figure 17. Upper-surface vorticity magnitude contours (indicating flow patterns) on the JSM for $\alpha = 18.58°$.

American Institute of Aeronautics and Astronautics
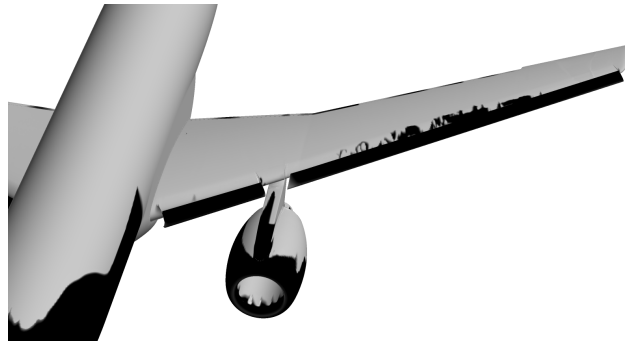
(a) China clay, front view [7]

(b) OVERFLOW surface turbulent index, front view

(c) China clay, rear view [7]
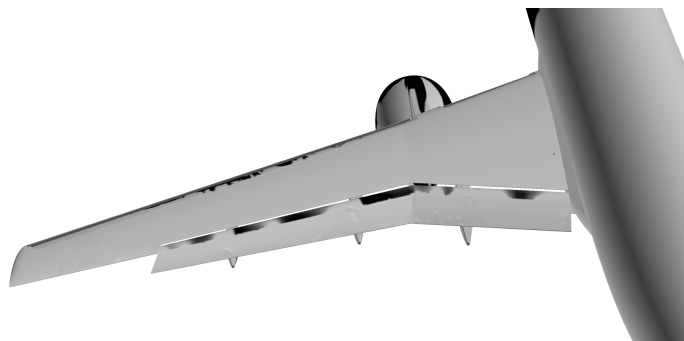
(d) OVERFLOW surface turbulent index, rear view

Figure 18. Upper-surface wing transition patterns on the JSM for $\alpha = 4.36°$.

(a)   China clay, front view [7]

(b)   OVERFLOW surface turbulent index, front view

(c)   China clay, rear view [7]

(d)   OVERFLOW surface turbulent index, rear view

Figure 19. Upper-surface wing transition patterns on the JSM for α = 10.47°.

American Institute of Aeronautics and Astronautics

(a) China clay, front view [7]

(b) OVERFLOW surface turbulent index, front view

(c) China clay, rear view [7]

(d) OVERFLOW surface turbulent index, rear view

Figure 20. Upper-surface wing transition patterns on the JSM for α = 18.58°.

American Institute of Aeronautics and Astronautics

V. Conclusion

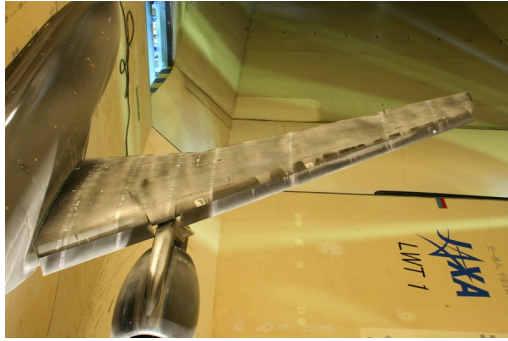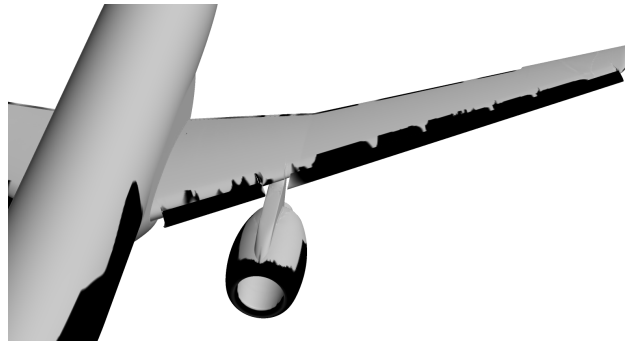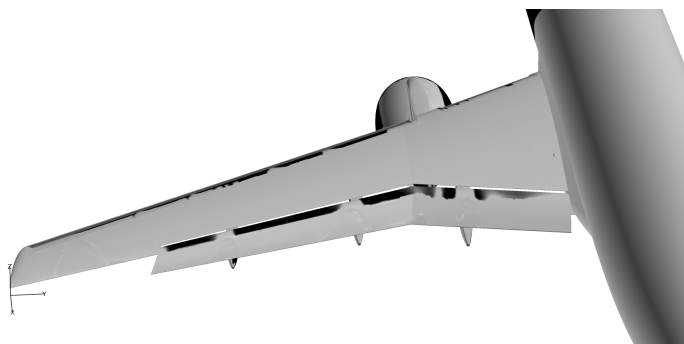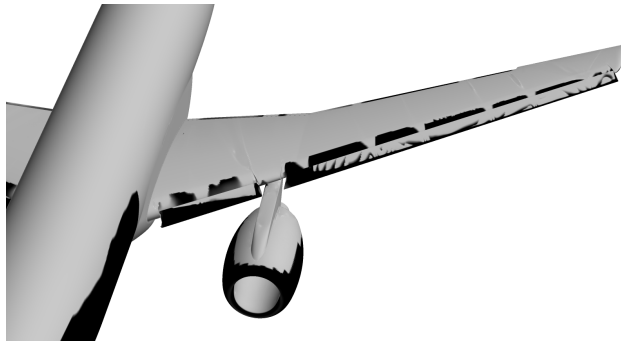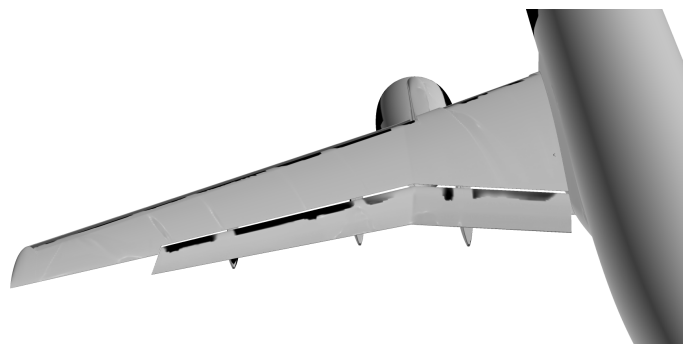Both the High-Lift Common Research Model (HL-CRM) and the JAXA Standard Model (JSM) were analyzed using the OVERFLOW and LAVA codes for the third High-Lift Prediction Workshop (HiLiftPW-3). For the HL-CRM cases, no experimental data are available yet, so all solutions are entirely predictive. Grid convergence studies were performed at two angles of attack, and the effect of the flap gap (full-chord or partially sealed) was investigated. For the unsealed, full-chord gap, the effects of turbulence modeling were explored, which showed a strong impact from using a quadratic constitutive relation. It was also observed that the smoothness of the surface representation in the grid generation process had an impact on the predictions. In the original committee-provided overset grids, the grids were projected back to a triangulation of the surface, which had coarser resolution than the grids and introduced spurious pressure oscillations. New grids were generated that projected directly back to the CAD surface, which produced smoother pressure distributions.

The JSM was studied for both the nacelle/pylon on and nacelle/pylon off, and solutions were generated using both fully turbulent methods and a predictive transition modeling method. For the nacelle/pylon off, whether the solutions were initialized from free stream ("cold start") or from a previously converged angle of attack ("warm start") had a strong impact on the solution, indicating that multiple solutions may exist. The cold starts generally resulted in premature stall and the solutions falling on a low-lift branch, while the warm starts produced a high-lift branch. In terms of physicality, the alpha-continuation effect of the warm start is more appropriate to how an actual aircraft is operated, but cold starts are more appropriate for industrial CFD analyses. This effect seemed to be limited to the use of QCR, as cold-start solutions without QCR fell on an ostensibly high-lift branch. When time accuracy was employed, the solutions followed the high-lift behavior.

Evidence of multiple solutions was not observed with the nacelle/pylon on, and all predictions followed high-lift behavior. As the multiple solutions are connected to the separation behavior of the wing, the presence of the nacelle and pylon effectively selects which separation behavior will occur. Consistent with the lack of multiple solutions, time accuracy did not have as strong of an impact with the nacelle/pylon on, except in the post-stall regime where strong, vortex-dominated separation prevails. Somewhat unexpectedly, the solution without QCR stalled earlier than those with QCR for this configuration, which is the opposite effect as was observed for the nacelle/pylon off.

Transition modeling effects were investigated for the JSM using a predictive, e^N-based transport equation method. Including transition had a positive impact on the force and moment predictions, and the predicted transition patterns were in strong agreement with those observed experimentally using China clay. Detailed investigation of the surface flow patterns and pressure distributions, however, revealed that some key discrepancies remain between the CFD and the experiment, even if the integrated quantities are in strong agreement. While transition modeling improved the predictions, it is not a panacea.

From these observations, there are some key takeaways for future high-lift aerodynamic analyses using computational fluid dynamics. First, grid generation should use a smooth representation of the surface geometry. Second, using solution restarts from lower angles of attack appears to be more reliable for obtaining a physically relevant solution, but for industrial practicality, time accuracy may be necessary. Third, the use of a quadratic constitutive relation is preferable for consistent solution behavior through configuration changes. Last, laminar-turbulent transition is non-negligible on these systems, and including predictive transition modeling in the simulation has a favorable impact on the predicted flow behaviors.

Appendix – AFT2017b Transition Model Definition

The AFT2017b laminar-turbulent transition model is an extension and enhancement of the amplification factor transport (AFT) transition model of Coder and Maughmer [22] and Coder [23]. As the full model definition has not yet appeared in a print publication, it is provided here for the benefit of the readers. AFT2017b is based on the solution of two scalar, transport equations for the amplification factor and modified intermittency. These transport equations are,

$$\frac{\partial(\rho\tilde{n})}{\partial t} + \frac{\partial(\rho u_j \tilde{n})}{\partial x_j} = \rho\Omega F_{crit}F_{growth}\frac{d\tilde{n}}{dRe_\theta} + \frac{\partial}{\partial x_j}\left[(\mu+\sigma_n\mu_t)\frac{\partial\tilde{n}}{\partial x_j}\right]$$

(A1)

and

American Institute of Aeronautics and Astronautics

$$\frac{\partial(\rho\tilde{\gamma})}{\partial t}+\frac{\partial(\rho u_j\tilde{\gamma})}{\partial x_j}=c_1\rho SF_{onset}\left[1-\exp(\tilde{\gamma})\right]-c_2\rho\Omega F_{turb}\left[c_3\exp(\tilde{\gamma})-1\right]+\frac{\partial}{\partial x_j}\left[\left(\mu+\frac{\mu_t}{\sigma_\gamma}\right)\frac{\partial\tilde{\gamma}}{\partial x_j}\right]$$

(A2)

respectively.

The amplification factor transport equation (Eq. A1) describes the growth and evolution of the approximate envelope amplification factor, which is a measure based on linear stability theory of how close a laminar boundary layer is to transition [26]. The source term is based on the evaluation of a localized boundary-layer shape factor (or pressure-gradient parameter) that is then used to estimate the corresponding integral properties. This local shape factor is based on the work of Menter [27] and is

$$H_L=\frac{d^2}{\mu}\left[\nabla(\rho\bar{u}\cdot\nabla d)\cdot\nabla d\right]$$

(A3)

It relates to the integral shape factor, H_{12} (displacement-to-momentum-thickness ratio), as,

$$H_{12}=0.376960+\sqrt{\frac{H_L+2.453432}{0.653181}}$$

(A4)

For numerical reasons, it is advantageous to limit H_L such that $-0.25\le H_L\le 200$. The functional dependencies of the source term are then

$$F_{crit}=\begin{cases}0, & Re_V<Re_{V,0}\\ 1, & Re_V\ge Re_{V,0}\end{cases}$$

(A5)

$$\frac{Re_{V,0}}{Re_{\theta,0}}=0.246175H_{12}^2-0.141831H_{12}+0.008886$$

(A6)

$$Re_V=\frac{\rho Sd^2}{\mu+\mu_t}$$

(A7)

$$\log_{10}\left(Re_{\theta,0}\right)=0.7\tanh\left(\frac{14}{H_{12}-1}-9.24\right)+\frac{2.492}{\left(H_{12}-1\right)^{0.43}}+0.62$$

(A8)

$$F_{growth}=\frac{H_{12}}{0.5482H_{12}-0.5185}\left[1+m(H_{12})\right]\frac{l(H_{12})}{2}$$

(A9)

$$l(H_{12})=\frac{6.54H_{12}-14.07}{H_{12}^2}$$

(A10)

$$m(H_{12})=\frac{1}{l(H_{12})}\left[0.058\frac{(H_{12}-4)^2}{H_{12}-1}-0.068\right]$$

(A11)

and

$$\frac{d\tilde{n}}{dRe_\theta} = 0.028\left(H_{12}-1\right) - 0.0345\exp\left[-\left(\frac{3.87}{H_{12}-1}-2.52\right)^2\right]$$

(A12)

The diffusion coefficient for the amplification factor is $\sigma_n = 1.0$.

Modified intermittency is the natural logarithm of the actual intermittency, which itself represents nearly binary logic as to whether the boundary-layer should be laminar ($\gamma = 0$) or turbulent ($\gamma = 1$). Through this transformation, the numerical bounds on the variable are alleviated without changing the sensitivity of the variable around the fully turbulent value. The model equation given in Eq. A2 is based heavily on the Menter intermittency model [27] with a non-linear diffusion term omitted through the change of variable. The source-term function definitions are

$$F_{onset,1} = \min\left(\frac{\tilde{n}}{N_{crit}},2\right)$$

(A13)

$$F_{onset,2} = \max\left[1-\left(\frac{\mu_t}{3.5\mu}\right)^3,0\right]$$

(A14)

$$F_{onset} = \max\left[F_{onset,1}-F_{onset,2},0\right]$$

(A15)

$$F_{turb} = \exp\left[-\left(\frac{\mu_t}{2\mu}\right)^4\right]$$

(A16)

Transition occurs when the transported amplification factor, $\tilde{n}$, reaches N_{crit}, which is the critical amplification factor. In this implementation, N_{crit} is calculated based on the free-stream turbulence intensity using a modified version of Mack's relation [28],

$$N_{crit} = -8.43 - 2.4\ln\left(\frac{\tau}{100}\right)$$

(A17)

$$\tau = 2.5\tanh\left(\frac{Tu_\infty(\%)}{2.5}\right)$$

(A18)

The use of the intermediary variable τ is based on the work of Drela to provide a smooth limiter to N_{crit} [29]. Without this step, negative values of N_{crit} are possible and lead to unwanted model behavior. Calibration coefficients for the modified intermittency equation are $c_1 = 100$, $c_2 = 0.06$, $c_3 = 50$, and $\sigma_\gamma = 1.0$, which come from Menter [27].

Boundary conditions for both the amplification factor and modified intermittency transport equations are both Dirichlet in the free stream and Neumann on solid walls as,

$$\tilde{n}_\infty = 0$$

(A19)

$$\tilde{\gamma}_\infty = 0$$

(A20)

$$\left.\frac{\partial\tilde{n}}{\partial y}\right|_{wall} = 0$$

(A21)

$$\left.\frac{\partial \tilde{\gamma}}{\partial y}\right|_{wall} = 0$$

(A22)

where y is taken to be the wall-normal direction.

The AFT2017b model interacts with the one-equation, Spalart-Allmaras (SA) turbulence model to provide a unified transition/turbulence modeling framework. The SA model is of the form,

$$\frac{D\tilde{v}}{Dt} = c_{b1}S\tilde{v}(1-f_{t2}) - \left(c_{w1}f_w - \frac{c_{b1}}{\kappa^2}f_{t2}\right)\left(\frac{\tilde{v}}{d}\right)^2 + \frac{1}{\sigma}\left\{\frac{\partial}{\partial x_j}\left[(v+\tilde{v})\frac{\partial \tilde{v}}{\partial x_j}\right] + c_{b2}\frac{\partial \tilde{v}}{\partial x_j}\frac{\partial \tilde{v}}{\partial x_j}\right\}$$

(A23)

and the AFT2017b model is coupled through the f_{t2} function as

$$f_{t2} = c_{t3}\left[1 - \exp(\tilde{\gamma})\right]$$

(A24)

This yields the SA-AFT2017b model, and common extensions of the SA model, such as the 'RC' correction and a quadratic constitutive relation (QCR) may be used the same as with the fully turbulent form and named accordingly (e.g. SA-RC-AFT2017b).

When used with the AFT2017b model, the wall boundary condition to the SA equation is unaltered from the fully turbulent form, and in the free-stream it is recommended that the modified eddy-viscosity ratio be 0.1 (actual eddy-viscosity ratio of 2.79 x 10^{-7}).

Acknowledgments

References

[1] Rumsey, C. L., Slotnick, J. P., Long, M., Stuever, R. A., and Wayman, T. R., "Summary of the First AIAA CFD High-Lift Prediction Workshop," *Journal of Aircraft*, Vol. 48, No 6, pp. 2068-2079.

[2] Rumsey, C. L. and Lee-Rausch, E. M., "NASA Trapezoidal Wing Computations Including Transition and Advnaced Turbulence Modeling," *Journal of Aircraft*, Vol. 52, No. 2, pp. 496-509.

[3] Rumsey, C. L. and Slotnick, J. P., "Overview and Summary of the Second AIAA High-Lift Prediciton Workshop*," Journal of Aircraft*, Vol. 52, No. 4, 2015, pp. 1006-1025.

[4] Coder, J. G., "OVERFLOW Analysis of the DLR-F11 High-Lift Configuration Including Transition Modeling," *Journal of Aircraft*, Vol. 52, No. 4, 2015, pp. 1082-1097.

[5] Rumsey, C. L., Slotnick, J. P., and Sclafani, A. J., "Overview and Summary of the Third AIAA High Lift Prediction Workshop," 56th AIAA Aerospace Sciences Meeting, Kissimmee, FL, January 2018.

[6] Lacy, D. S. and Sclafani, A. J., "Development of the High Lift Common Research Model (HL-CRM): A Representative High Lift Configuration for Transonic Transports", 54th AIAA Aerospace Sciences Meeting, AIAA Paper 2016-0308, San Diego, CA, Jan. 2016.

[7] Yokokawa, Y., Murayama, M., Ito, T., and Yamamoto, K., "Experiment and CFD of a High-lift Configuration Civil Transport Aircraft Model," 25th AIAA Aerodynamic Measurement Technology and Ground Testing Conference, AIAA Paper 2006-3452, San Francisco, CA, June 2006.

[8] Yokokawa, Y., Murayama, M., Kanazaki, M., Murota, K., Ito, T., and Yamamoto, K., "Investigation and Improvement of High-lift Aerodynamic Performances in Lowspeed Wind Tunnel Testing," 46th AIAA Aerospace Sciences Meeting, AIAA Paper 2008-0350, Reno, NV, January 2008.

[9] Vassberg, J. C., Dehaan, M. A., Rivers, M., and Wahls, R. A., "Development of a Common Research Model for Applied CFD validation Studies," 26th AIAA Applied Aerodynamics Conference, AIAA 2008-6919, Honolulu, HI, Aug. 2008.

[10] Vassberg, J. C. et al., "Summary of the Fourth AIAA Computational Fluid Dynamics Drag Prediction Workshop," *Journal of Aircraft*, Vol. 51, No. 4, 2014, pp. 1070-1089.

[11] Levy, D. W. et al., "Summary of Data from the Fifth AIAA Computational Fluid Dynamics Drag Prediction Workshop," *Journal of Aircraft*, Vol. 51, No. 4, 2014, pp. 1194-1213.

[12] Tinoco, E. N., Brodersen, O., Keye, S., and Laflin, K., "Summary of Data from the Sixth AIAA CFD Drag Prediction Workshop: CRM Cases 2 to 5," 55th AIAA Aerospace Sciences Meeting, AIAA Paper 2017-1208, Grapevine, TX, January 2017.

[13] Chawner, J. and Woeber, C., Geometry and Mesh Generation Workshop Website, https://pointwise.com/gmgw.

American Institute of Aeronautics and Astronautics

[14] Chan, W., "Best Practices on Overset Structured Mesh Generation for the High-Lift CRM Geometry," 55th AIAA Aerospace Sciences Meeting, AIAA 2017-0362, Grapevine, Texas, Jan. 2017.

[15] "ANSA: The Advanced CAE Pre-processing Software for Complete Model Build-up," BETA CEA Systems (https://www.beta-cae.com/ansa.htm), 2016.

[16] Jensen, J. C., Denison, M., Stitch, G.-D., Housman, J., and Kiris, C., "LAVA Simulations for the 3rd AIAA CFD High Lift Prediction Workshop with Body Fitted Grids", 55th AIAA Aerospace Sciences Meeting, Kissimmee, FL, Jan. 2018.

[17] Nichols, R. H. and Buning, P. G., "User's Manual for OVERFLOW 2.2, Version 2.2m," NASA Langley Research Center, Hampton, VA, October 2017.

[18] Pandya, S., Venkateswaran, S., and Pulliam, T. H., "Implementation of Preconditioned Dual-Time Procedures in OVERFLOW," 41st AIAA Aerospace Sciences Meeting, AIAA Paper 2003-0072, Reno, NV, January 2003.

[19] Spalart, P. R. and Allmaras, S. R., "A One-Equation Turbulence Model for Aerodynamic Flows," *La Recherche Aerospatiale*, No. 1, 1994, pp. 5-21.

[20] Shur, M. L., Strelets, M. K., Travin, A. K., Spalart, P. R., "Turbulence Modeling in Rotating and Curved Channels: Assessing the Spalart-Shur Correction," *AIAA Journal*, Vol. 38, No. 5, 2000, pp. 784-792.

[21] Spalart, P. R., "Strategies for Turbulence Modelling and Simulation," *International Journal of Heat and Fluid Flow*, Vol. 21, 2000, pp. 252-263

[22] Coder, J. G. and Maughmer, M. D., "Computational Fluid Dynamics Compatible Transition Modeling Using an Amplification Factor Transport Equation," *AIAA Journal*, Vol. 52, No. 11, pp. 2506-2512.

[23] Coder, J. G., "Enhancement of the Amplification Factor Transport Transition Modeling Framework," 55th AIAA Aerospace Sciences Meeting, AIAA Paper 2017-1709, Grapevine, TX, Jan. 2017.

[24] Kiris, C., Housman, J., Barad, M., Brehm, C., Sozer, E., and Moini-Yekta, S., "Computational Frameworkk for Launch, Ascent, and Vehicle Aerodynamics (LAVA)", *Aerospace Science and Technology*, Vol. 55, August 2016, pp. 189-219.

[25] Steger, J.L. and Benek, J.A., "On the Use of Composite Grid Schemes in Computational Aerodynamics", NASA TM-88372, 1986.

[26] Drela, M. and Giles, M. B., "Viscous-Inviscid Analysis of Transonic and Low Reynolds Number Airfoils," *AIAA Journal*, Vol. 25, No. 10, 1987, pp. 1347-1355.

[27] Menter, F. R., Smirnov, P. E., Liu, T., and Avancha, R., "A One-Equation Local Correlation-Based Transition Model," *Flow, Turbulence and Combustion*, Vol. 95, No. 4, 2015, pp. 583-619.

[28] Mack, L. M., "Transition and Laminar Instability," NASA CR-153203, 1977.

[29] Drela, M., "MISES Implementation of Modified Abu-Ghannam/Shaw Transition Criterion (Second Revision)", Massachusetts Institute of Technology Dept. of Aeronautics and Astronautics, July 1998.

American Institute of Aeronautics and Astronautics